International Communications in Heat and Mass Transfer 180 (2026) 112409

Contents lists available at ScienceDirect

International Communications in Heat and Mass Transfer

journal homepage: www.elsevier.com/locate/ichmt

Dual-channel modular phase change material thermal energy storage inspired by plate heat exchangers: ANN-assisted optimization using a multilayer perceptron

Yonghui Li [a], Ali Basem [b], Mohammad Nadeem Khan [c], Teeba Ismail Kh [d], Haibo Zhang [a,*], Norah Alsairy [e], Ashrf Althbiti [f], Zafar Rakhmanov [g], Hind Albalawi [h,*], Ibrahim Mahariq [i,j,k,**]

[a] School of Digital Economy and Management, Sichuan Technology and Business University, Meishan, Sichuan 620000, China
[b] Advanced Technical College, University of Warith Al-Anbiyaa, Karbala, Iraq
[c] Department of Mechanical and Industrial Engineering, College of Engineering, Majmaah University, Al-Majmaah 11952, Saudi Arabia
[d] Department of Computer Engineering, College of Engineering and Computer Science, Lebanese French University, Erbil, Kurdistan Region, Iraq
[e] Department of Physics, College of Turabah, Taif University, P.O. Box 11099, Taif 21944, Saudi Arabia
[f] Department of Information Technology, College of Computers and Information Technology, Taif University, Taif 21944, Saudi Arabia
[g] School of Exact Sciences, National Pedagogical University of Uzbekistan named after Nizami, Tashkent, Uzbekistan
[h] Department of Physics, College of Sciences, Princess Nourah bint Abdulrahman University, P.O. Box 84428, Riyadh 11671, Saudi Arabia
[i] Department of Electrical and Electronic Engineering, Faculty of Engineering and Architecture, Istanbul Gelisim University, Avcılar-Istanbul, 34310 Istanbul, Türkiye
[j] Department of Medical Research, China Medical University Hospital, China Medical University, Taichung, Taiwan
[k] University College, Korea University, Seoul 02481, South Korea

ARTICLE INFO

Keywords:
Solar-driven resources
Thermal energy storage
Heat transfer fluid channel
Multilayer perceptron
Prediction model
Phase change material

ABSTRACT

The growing integration of renewable energy systems has heightened the demand for efficient thermal energy storage technologies to balance energy supply and demand. Phase change material (PCM)-based latent heat storage systems are attractive owing to their significant energy storage density and nearly isothermal operation; nevertheless, conventional configurations often suffer from low heat transfer rates, non-uniform melting, and limited scalability. In many heat-exchanger-inspired designs, heat transfer fluid (HTF) channels are located only along the outer boundaries of the PCM enclosure, leaving the central region thermally underutilized. To mitigate these drawbacks, the current work develops a novel modular energy storage system inspired by plate heat exchanger architecture. The system consists of 60 independent units that allow flexible assembly and scalable storage capacity. A key innovation is the incorporation of an additional HTF channel inside the PCM enclosure, forming two parallel heat transfer paths that enhance the effective heat transfer surface and decrease thermal resistance. To accelerate the design process, a multilayer perceptron surrogate model was developed to anticipate stored energy during charging. A two-stage optimization framework based on a genetic algorithm and the TOPSIS method was applied to identify the optimal configurations. The optimized designs demonstrated remarkably better performance than the reference configuration. At 9000 s, the half-time optimized design stored the largest amount of energy, reaching 9402 kJ, followed closely by the balanced design, which stored 9287 kJ, while the full-time optimized design stored 8654 kJ. In comparison, the core design stored only 3818 kJ at the same time. Compared with the core design, the stored energy improved by approximately 146% for the half-time optimized design, 126.6% for the full-time optimized design, and 143.2% for the balanced design. At the end of the melting process (18,000 s), the liquid fractions were 0.9649 for the half-time optimized design, 1 for both the full-time optimized design and the balanced design, and 0.3745 for the reference configuration. Correspondingly, the stored energy increased from 6457 kJ in the core design to 12,585 kJ, 13544 kJ, and 13,113 kJ for the half-time optimized design, full-time optimized design, and balanced design, respectively, representing improvements of up to 109.8%.

* Corresponding authors.
** Corresponding author at: Department of Electrical and Electronic Engineering, Faculty of Engineering and Architecture, Istanbul Gelisim University, Avcılar-Istanbul, 34310 Istanbul, Türkiye.
E-mail addresses: SCI868@126.com (H. Zhang), hmalbalawi@pnu.edu.sa (H. Albalawi), ibmahariq@gmail.com (I. Mahariq).

https://doi.org/10.1016/j.icheatmasstransfer.2026.112409

Available online 10 September 2026

1. Introduction

Nomenclature

C_p	specific heat (kJ/kg·K)
CH	inner HTF channel' height (mm)
CS	inner HTF channel' space between inlet and outlet (mm)
D_h	hydraulic diameter (m)
F	latent enthalpy of melting (kJ/kg)
h	sensible enthalpy (kJ/kg)
I	characteristic height (m)
k	thermal conductivity (W/m·k)
M_c	mushy zone constant
P	pressure (Pa)
Ra	Rayleigh number
Re	Reynolds number
t	time (s)
T	temperature (K)
T_0	liquidus temperature of the PCM (K)
u	velocity in x direction (m/s)
v	velocity in y direction (m/s)
ε	constant computational parameter
α	source term
θ	angle of the inner HTF channel (degree)
φ	liquid fraction
β	coefficient of thermal expansion (1/K)

Abbreviations

CC	closeness coefficient
GA	genetic algorithm
HTF	heat transfer fluid
MLP	multi-layer perceptron
PCM	phase change material
RMSE	root mean square error

Thermal energy constitutes the dominant share of global final energy consumption. According to assessments by the International Energy Agency, heat accounts for almost 50% of the whole energy demand worldwide, exceeding the shares of electricity and transport fuels individually [1]. This demand arises primarily from industrial processes, space heating and cooling in buildings, domestic hot water production, and district energy systems [2]. Despite its central role, thermal energy systems still rely heavily on fossil fuels, leading to significant greenhouse gas emissions and exposing energy infrastructures to fuel price volatility [3]. This situation, therefore, represents both a critical decarbonization challenge and a strategic opportunity for renewable integration [4].

However, the transition toward sustainable thermal systems is constrained by the temporal mismatch between supply and end-use demand [5]. Solar-driven thermal resources are inherently intermittent and variable due to geographic location, time of day, and seasonal fluctuations [6]. This structural imbalance necessitates the deployment of efficient thermal energy storage technologies capable of storing surplus energy and delivering it when direct generation is insufficient [7]. Among the available storage options, latent-based energy storage systems have been in the spotlight due to their superior energy density and nearly isothermal operation [8]. By selecting phase change materials (PCMs) as the base storage medium, these systems exploit the latent heat of solid-liquid phase transitions to absorb and release noticeable amounts of energy over a narrow temperature interval [9]. During charging, thermal energy is stored as the PCM undergoes melting at its characteristic phase transition temperature [10]. Because the majority of the absorbed energy contributes to the phase transformation rather than to temperature rise, large storage capacities can be achieved without significant thermal gradients [11]. Upon discharge, the reverse solidification process releases the stored latent heat at nearly constant temperature, ensuring stable and controllable heat output [12]. Nevertheless, most PCM-based setups suffer from restricted heat transfer performance, which can lead to slow charging and discharging rates [13]. This limitation also results in non-uniform temperature distribution, incomplete phase transition within practical operating times, and reduced effective storage capacity under dynamic conditions [14].

Several approaches have been developed to promote the thermal conductivity of PCMs and improve system efficiency [15]. The first technique consists of adding high-thermal-conductivity additives to the material, forming composite or enhanced PCMs [16]. Materials such as graphite powders, metal foams, or graphene-based nanoparticles are embedded within the storage medium to create conductive pathways [17]. These inclusions significantly reduce thermal resistance and promote faster heat penetration during both energy absorption and release [18]. The second technique is encapsulation at the micro- or macro-scale [19]. By enclosing the PCM within a containment shell, encapsulation prevents leakage during melting, enhances surface-area-to-volume ratio, and maintains mechanical stability during repeated thermal cycles [20]. The third strategy focuses on geometry-based heat transfer enhancement, commonly referred to as extended or auxiliary surfaces [21]. In this method, structures such as ribs, fins, or channel networks are designed to be incorporated within the PCM domain to expand the effective heat transfer area [22]. These inserts accelerate energy exchange between the PCM and the heat transfer fluid (HTF), thereby shortening charging and solidification durations [23]. Compared with material modification and encapsulation techniques, extended surfaces are often preferred by researchers due to their lower cost, simpler fabrication, and ease of integration into conventional thermal storage configurations [24].

Yan et al. [25] developed a rib-enhanced PCM domain to reduce melting time in an energy storage system. Eight aluminum ribs were utilized, and multiple geometric arrangements were assessed by varying rib angles and spacing to determine the optimal design. The analysis showed that complete melting in the rib-free case occurred after 19,648 s, which was 118.2% longer than the optimized system. It also needed 130.5% and 129.4% more time to reach 50% and 80% charging, respectively. Han et al. [26] conducted a comparative study of annular, longitudinal, and composite fins with identical total fin volume. They altered the fin number and dimensions to evaluate the influence of several volumetric ratios within the composite design. The findings indicated that composite fins ameliorated thermal performance compared with single-type fins. Under number variation, optimal performance was obtained at a 50%–50% volumetric ratio. However, dimension variation yielded superior results when annular fins accounted for 37.5% of the total volume. In this case, the melting time decreased by 6.75%, and the heat storage rate increased by 7.60%. Tang et al. [27] examined the effect of discontinuous fin configurations on PCM discharging behavior. The main fin length and bifurcation angle were identified as the key parameters controlling the optimized arrangement. The results demonstrated that fins with a length of 15 mm and a bifurcation angle of 0.45 accelerated solidification time by 22.14% and enhanced heat release rate by 28.45% relative to traditional longitudinal fins. Mao et al. [28] proposed triangular rib structures to promote the thermal specifications of a PCM-based thermal storage

device. Their design was evaluated against a baseline model without ribs. The novel energy storage device exhibited superior melting behavior, achieving complete phase change in under 5 h, while the reference system attained only 48% liquid fraction within the same duration. In addition, the ribbed component resulted in an approximate 75% increase in stored energy relative to the baseline setup. Song et al. [29] optimized fin layouts by modifying the geometry of HTF channels. Different structural types, including circular, elliptical, square, and triangular, were analyzed to investigate the impact of their geometries on thermal characteristics. It was determined that circular and elliptical shapes generated radial conductive skeletons with elongated backbones and sparse branching, whereas square and triangular shapes produced dense, tree-like networks. It was reported that the triangular channel configuration provided superior performance, with a 33.4% improvement rate and a minimum phase transition time of 89.6 min.

In recent years, the multi-layer perceptron (MLP) approach has been applied to analyze the functionality of energy storage systems [30]. Its popularity stems from the ability to simulate highly nonlinear relationships between design variables and thermal characteristics without requiring explicit analytical formulations [31]. Compared with conventional numerical simulations, MLP leads to notable savings in computational time and avoids the high resource demands of fine-mesh modeling [32]. Unlike traditional regression or empirical methods, it is less sensitive to data dispersion and can maintain predictive capability even when the dataset contains noise or incomplete trends [33]. MLP networks can estimate phase change behavior, heat transfer rates, and temperature distributions, making them a flexible tool for optimizing energy storage units. Abdellatif et al. [34] employed an MLP model to examine the heat transfer performance in four PCM enclosures. A rectangular box with three inclined walls at 30°, 45°, and 60° was investigated. The study demonstrated that the rectangular container exhibited the longest melting time of 11,040 s. Introducing wall inclinations progressively reduced the melting duration to 9200 s, 8440 s, and 8200 s for 30°, 45°, and 60°, respectively. Vaferi et al. [35] explored optimization of a latent energy storage system by adjusting the placement and angles of finned tubes to enhance natural convection. MLP prediction models combined with a genetic algorithm were used to determine the optimal system configurations. Two configurations were identified: the first minimized the period to achieve 50% PCM charging, and the second minimized the period to reach 94% charging. The two optimal structures outperformed the finless model, resulting in PCM charging increases of 25.12% and 28.06%, respectively.

Although numerous studies have investigated PCM-based thermal energy storage systems, most conventional designs rely on single-sided heat transfer enhancement and suffer from non-uniform melting and limited scalability. In particular, systems inspired by compact heat exchangers often utilize HTF channels only along the outer boundary of the PCM enclosure, leaving the central region thermally underutilized. Moreover, the integration of intelligent modeling and systematic optimization into the structural design of such systems remains insufficiently explored. The present study introduces a novel plate-heat-exchanger-inspired energy storage system that simultaneously addresses structural efficiency, modularity, and optimization. The proposed system consists of 60 independent units, enabling simple transportation, flexible assembly, and straightforward adjustment of PCM capacity in response to energy demand. Unlike traditional fixed-geometry storage devices, this modular architecture provides scalability without redesigning the entire system. The key structural innovation is to embed an additional HTF channel within the PCM enclosure, creating two parallel HTF flow paths: one surrounding the PCM and the other penetrating its center. This dual-channel configuration significantly enhances the available heat transfer surface area and reduces thermal resistance inside the PCM region. Furthermore, by dividing the PCM region into two thermally active sections, the design enables the use of two distinct PCMs with different melting temperatures within a single unit. Beyond geometric innovation, this work integrates a high-accuracy MLP model to predict stored energy at intermediate and final charging stages. This surrogate model replaces repetitive numerical simulations and forms the basis for intelligent optimization. Finally, a two-stage genetic algorithm framework comprising single- and multi-objective optimization was implemented to identify configurations that maximize energy storage performance.

2. Geometry and structural configuration of the proposed system

Fig. 1 depicts the overall architecture and geometric details of the proposed modular PCM-based energy storage system. The figure is divided into three subfigures to clearly present the assembled device, the modular arrangement, and the cross-sectional geometry of a representative unit. Fig. 1a shows the assembled storage module, composed of multiple parallel plates that form a compact rectangular structure. The HTF, which is water in the present study, enters the system through the inlet port located on one side of the frontal plate and exits through the outlet port positioned on the opposite side. Fig. 1b presents the exploded view of the system, highlighting its modular design. The number of PCM units was selected based on a practical design consideration rather than being treated as an optimization parameter. In the present study, the target was to develop a storage module with an overall length of approximately 1 m. Based on the dimensions of the proposed unit, assembling 60 identical units (each with 17 mm length) produced a total module length of approximately 1020 mm, which satisfied this design objective. Owing to the modular nature of the proposed concept, the total length of the storage system can be readily adjusted by increasing or decreasing the number of units. Consequently, the proposed design is scalable, allowing shorter or longer storage modules to be constructed for different engineering applications without modifying the geometry of the individual units. Within each module, an inner HTF channel is embedded in the conductive body, while an outer channel surrounds the PCM enclosure, enabling enhanced heat transfer between the HTF and the storage medium.

From a manufacturing perspective, the proposed storage system is composed of identical modular units that are assembled to form the complete thermal energy storage module. Since each unit contains both inner and outer HTF channels, high dimensional accuracy is required to ensure proper alignment between neighboring modules. Consequently, high-precision manufacturing techniques, such as CNC machining or cold extrusion, are recommended to accurately fabricate the proposed geometry. Although these methods increase manufacturing cost, they also improve assembly quality and facilitate reliable sealing between the PCM and HTF domains. Reliable sealing can be achieved by connecting adjacent HTF channels using precisely machined sleeves (bushings) or similar mechanical connectors that provide both accurate alignment and leak-tight interfaces. Furthermore, because the operating temperature range of the proposed latent heat storage system is relatively moderate, significant thermal expansion is not anticipated. Nevertheless, to accommodate small differential thermal expansions during repeated thermal cycles and to reduce mechanical stresses at the interfaces, a thin gasket may be placed between adjacent modules. This compliant sealing layer can compensate for minor dimensional changes while enhancing the long-term mechanical integrity and sealing performance of the modular system. Fig. 1c illustrates the cross-sectional geometry of a single storage unit and compares three channel configurations with inclination angles of $\theta = 80°$, 90°, and 100°. The outer red boundary represents the outer HTF channel that forms the PCM enclosure, while the inner red passage corresponds to the central HTF channel. The hydraulic diameter of the HTF channels is 15 mm. The blue region indicates the PCM domain, where RT50 is used as the phase change material. The enclosure's total height is 335 mm, and its width is 270 mm. The wall thickness is 15 mm, and the clearance between internal features is 1 mm.

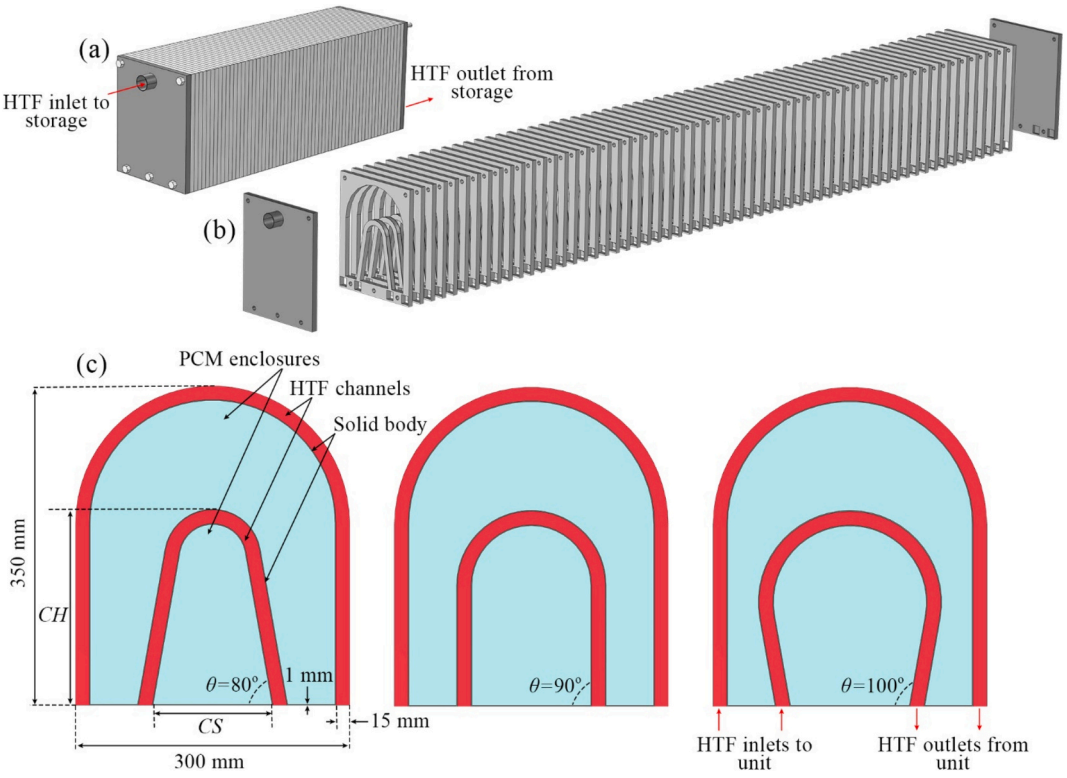

Fig. 1. (a) Assembled view of the proposed energy storage system showing HTF inlet and outlet ports; (b) Exploded view illustrating the modular arrangement of 60 individual storage units; (c) Cross-sectional geometry of a representative unit showing PCM enclosure, outer and central HTF channels, geometric parameters, and different channel inclination angles (θ = 80°, 90°, and 100°).

3. Numerical simulation

3.1. Phase change modeling method

By implementing the enthalpy-porosity procedure in simulations of PCM-based systems, natural convection effects can be accurately captured. In this framework, the latent heat associated with melting and solidification is embedded within the energy balance via an enthalpy term, allowing the phase transition to be handled implicitly. The state of the material is described by a liquid fraction that continuously evolves from 0 (solid) to 1 (liquid), eliminating the need to resolve the moving phase boundary explicitly. Zones with intermediate liquid fraction are treated as a resistive medium known as the mushy region. In this region, the coexistence of solid and liquid phases restricts fluid motion and behaves similarly to a porous structure. To account for this resistance, a momentum-damping term based on the Darcy permeability formulation is incorporated into the momentum equations. The resistance's strength is governed by the mushy zone constant (M_c). Here, the M_c value is set to 10^6, effectively suppressing unrealistic velocities in partially solidified regions.

3.2. Governing equations and related assumptions

To facilitate the numerical analysis while preserving the dominant physical mechanisms of the system, the following simplifications are considered:

- Flow characteristics

The heat transfer and flow processes are assumed to be 2D, transient, and incompressible. Based on the operating conditions, the flow regime in the HTF channels remains laminar. The Reynolds number of the HTF is approximately 1569, which is lower than the critical value of 2300 for transition to turbulence. Similarly, the natural convection flow of the molten PCM is assumed to be laminar, as the Rayleigh number is below the critical value of 10^9 [36].

- Thermo-physical properties

All materials are assumed homogeneous and isotropic, with constant properties in each phase during the computation (Table 1). However, density variations in the liquid RT50 are accounted for applying the Boussinesq approximation to capture buoyancy-driven natural convection. This approach allows density to vary only in the buoyancy term of Eq. (5) while maintaining it constant elsewhere [36].

- Energy dissipation and body forces

Viscous dissipation is omitted from the analysis due to its insignificant effect on the overall energy balance. A uniform gravitational acceleration (g) of 9.81 m/s^2 is considered downward along the vertical axis.

The flow regime inside the HTF channels is evaluated using the Reynolds number (Re) [40].

Table 1
Required data for materials.

Properties	RT50 [37]		Water (at 333.15 K) [38]	Aluminum [39]
	Solid	Liquid		
ρ (kg/m^3)	880	760	983	2719
C_p (J/kg·K)	2000	2000	4183	871
k (W/m·K)	0.2	0.2	0.641	202.4
μ (kg/m·s)	–	0.0038	0.00047	–
β (1/K)	0.0006		–	–
F (J/kg)	168,000		–	–
T_m (K)	318.15–324.15		–	–

$$Re = \frac{\rho V D_h}{\mu} \tag{1}$$

Rayleigh number (Ra) represents the balance between buoyancy forces and resistive effects (viscosity and thermal diffusion) in a fluid. Higher values of Ra mean stronger natural convection currents [41].

$$Ra = \frac{g\beta C_p \rho^2 (T_{HTF} - T_{PCM}) l^3}{\mu k} \tag{2}$$

The conservation of mass for incompressible flow is expressed as [42]:

$$\frac{\partial u}{\partial x} + \frac{\partial v}{\partial y} = 0 \tag{3}$$

This relation maintains mass conservation within each control volume throughout the transient melting process. The momentum transport in the horizontal direction is described as [43]:

$$\rho_{0,l}\left(\frac{\partial u}{\partial t} + u\frac{\partial u}{\partial x} + v\frac{\partial u}{\partial y}\right) = -\frac{\partial P}{\partial x} + \mu\left(\frac{\partial^2 u}{\partial x^2} + \frac{\partial^2 u}{\partial y^2}\right) + \alpha_x \tag{4}$$

where P represents pressure, and α_x denotes the momentum damping term associated with the enthalpy-porosity method. This term suppresses fluid motion within solid or partially solidified PCM regions. Similarly, the vertical momentum balance is given by Eq. (5) [44].

$$\rho_{0,l}\left(\frac{\partial v}{\partial t} + u\frac{\partial v}{\partial x} + v\frac{\partial v}{\partial y}\right) = -\frac{\partial P}{\partial y} + \mu\left(\frac{\partial^2 v}{\partial x^2} + \frac{\partial^2 v}{\partial y^2}\right) + g\rho_{0,l}(1 - \beta(T - T_0)) + \alpha_y \tag{5}$$

where the buoyancy force term $g\rho_{0,l}(1 - \beta(T - T_0))$ accounts for density variations caused by temperature differences according to the Boussinesq approximation. This term accounts for natural convection within the molten PCM. The variable T_0 used in the buoyancy term of Eq. (5) is equivalent to the liquidus temperature T_l, representing the temperature at which the PCM begins to melt and liquid PCM is formed. The conservation of energy in the PCM is indicated as follows [45]:

$$\rho_{0,l}\left(\frac{\partial H}{\partial t} + u\frac{\partial H}{\partial x} + v\frac{\partial H}{\partial y}\right) = k_l\left(\frac{\partial^2 T}{\partial x^2} + \frac{\partial^2 T}{\partial y^2}\right) \tag{6}$$

This formulation allows the phase transition to be captured implicitly during melting. For the solid structural materials of the PCM enclosure, the heat transfer process is governed by Eq. (7) [46].

$$\rho_s C_{P,s}\frac{\partial T}{\partial t} = k_s\left(\frac{\partial^2 T}{\partial x^2} + \frac{\partial^2 T}{\partial y^2}\right) \tag{7}$$

where the subscript s denotes the thermo-physical properties of the solid surfaces. The above conservation equations are applied to both the PCM and HTF regions. However, in the HTF domain, the buoyancy-related Boussinesq term and the momentum-damping source terms are omitted because the inlet velocity and phase change forces prevent the flow from occurring in the fluid channel. The specific enthalpy is expressed as [47]:

$$H = h + \Delta H \tag{8}$$

$$h = h_{ref} + \int_{T_{ref}}^{T} C_p dT \tag{9}$$

$$\Delta H = \varphi F \tag{10}$$

where h_{ref} is the reference enthalpy at temperature T_{ref}. The liquid fraction is determined from the PCM temperature [48].

$$\varphi = \begin{cases} 0 & if \quad T_{PCM} < T_s \\ \dfrac{T_{PCM} - T_s}{T_l - T_s} & if \quad T_s \le T_{PCM} \le T_l \\ 1 & if \quad T_{PCM} > T_l \end{cases} \tag{11}$$

where T_s denotes the solidus temperature of the PCM, respectively. The resistance applied via the solid matrix in the mushy zone is modeled using Eqs. (12)–(14) [49].

$$\alpha_x = -A(\varphi)u \tag{12}$$

$$\alpha_y = -A(\varphi)v \tag{13}$$

$$A(\varphi) = M_c\frac{(1-\varphi)^2}{\varphi^3 + \varepsilon} \tag{14}$$

where $A(\varphi)$ is the permeability function. The energy storage performance of the proposed unit is evaluated using the transient melting enhancement ratio (*TMER*). This parameter quantifies the improvement in the melting process of the modified configuration relative to a reference case. A higher *TMER* value indicates that the PCM melts more rapidly compared with the core design [50].

$$TMER = \left[\frac{\varphi}{\varphi_{cd}} - 1\right] \times 100\% \tag{15}$$

where φ_{cd} corresponds the core design, indicating the system in the absence of an inner HTF channel. The total stored energy is one of the most important performance indicators in thermal energy storage systems, representing the total thermal energy stored by the PCM during the charging process. It can be expressed as follows:

$$\begin{aligned} Q_{total} &= Q_{sensible} + Q_{latent} \\ &= \varphi\rho_l \forall C_{P,l}\Delta T_{sensible,l} + (1-\varphi)\rho_s \forall C_{P,s}\Delta T_{sensible,s} + \varphi\rho_l \forall F \end{aligned} \tag{16}$$

Here, Q_{total} represents the total stored energy absorbed by the PCM. $\forall$ denotes the net volume of the PCM enclosure. The hydraulic performance of the system was evaluated through the pumping power required to circulate the heat transfer fluid. The pumping power is defined as [51]:

$$PP = \dot{\forall}\Delta P \tag{17}$$

where ΔP is the total pressure drop across the system and $\dot{\forall}$is the volumetric flow rate of the heat transfer fluid. This formulation enables a direct assessment of the energetic cost associated with fluid circulation in the proposed thermal energy storage system.

3.3. Boundary and initial conditions

- Velocity boundary condition: The HTF enters the channels with a uniform velocity of 0.05 m/s.
- Inlet temperature: The HTF temperature at the channel inlets is maintained at 333.15 K.
- Outlet condition: A zero-gauge pressure boundary condition is imposed at the outlets of the HTF channels.
- Wall condition: All solid surfaces satisfy the no-slip velocity condition and the no-temperature-jump assumption at the solid-fluid interfaces.
- Pressure level: The operating pressure is fixed at 1 atm.
- Initial temperature: At $t = 0$, the temperature of the solid structure and the PCM is 298.15 K.

3.4. Numerical methodology and solution strategies

The plate-storage system was modeled using ANSYS Fluent as the computational platform. The SIMPLE approach was employed for

pressure-velocity coupling, ensuring stability in the iterative solutions. A second-order upwind discretization was exerted to Eqs. (4)–(7) to enhance numerical precision. The PRESTO method was used for pressure interpolation, which is especially effective in buoyancy-driven flows. To improve convergence, under-relaxation factors were set to 0.3 for pressure, 0.7 for momentum, 0.9 for liquid fraction, and 1.0 for density and energy. The simulations were carried out until the residuals of all equations were reduced to 10^{-6}.

4. Verification of PCM melting simulation

To evaluate the capability of the developed numerical model, the present simulation results were validated against the experimental study conducted by Kamkari and Groulx [52]. In their work, the energy absorption performance of a PCM was examined under both horizontal and vertical orientations. The setup consisted of a rectangular container measuring 120 × 50 × 120 mm, filled with PCM initially at 25 °C. The melting process was started by imposing a constant temperature of 60 °C on the finned wall of the enclosure, while the ambient temperature remained at 25 °C. According to the uncertainty analysis reported in the reference work, the maximum uncertainties associated with the measured liquid fraction and heat transfer rate were approximately 4.2% and 8.2%, respectively.

Fig. 2a and b compare the liquid fraction obtained from the present numerical results compared against the experimental measurements for the horizontal and vertical configurations, respectively. As observed, the acquired liquid fraction closely follows the reference trend during the entire melting process for both orientations. Small deviations observed during the intermediate phases are likely due to experimental uncertainties as well as the assumptions incorporated in the proposed model. Hence, the overall agreement between the numerical and experimental findings confirms that the presented computational framework can reliably capture the dominant heat transfer mechanisms governing PCM melting. A sensitivity analysis of M_c is carried out using three commonly adopted mushy zone constants (10^5, 10^6, and 10^7). The results indicate that M_c of 10^6 provides the best overall agreement with the experimental liquid-fraction evolution for both the horizontal and vertical rectangular enclosures. When M_c is reduced to 10^5, the numerical model predicts a slightly faster melting process, leading to an overestimation of the liquid fraction. Increasing the M_c to 10^7 suppresses the flow within the mushy region more strongly, resulting in a slightly slower melting process. It is also observed that the difference between the predictions obtained with M_c 10^6 and 10^7 is relatively small compared with that between 10^5 and 10^6. This behavior indicates that the numerical solution gradually becomes insensitive to further increases in the M_c, demonstrating convergence toward M_c-independent results.

The charging pattern of the PCM is indicated in Fig. 2c and d, where the phase interface acquired from the present simulations is compared with the experimentally observed ones at several time instants. The results demonstrate a strong similarity between the predicted and measured melting fronts. Initially, the charging is dominated via heat conduction. As the liquid region grows, buoyancy-driven natural convection develops within the molten PCM, driving movement of the warmer fluid and accelerating charging in the upper region of the enclosure. The numerical model successfully reproduces these physical phenomena and accurately predicts the evolution of the melting front over time. Fig. 2e and f present the second validation case, performed using the experimental study of Kousha et al. [53], in which the PCM is contained in a circular enclosure heated by three internal tubes. Fig. 2e compares the temporal evolution of the average PCM temperature predicted by the present numerical model with the experimental measurements, demonstrating excellent agreement throughout the melting process. Fig. 2f further compares the experimentally observed melting fronts with the corresponding numerical predictions at different charging times. The close agreement between the experimental and numerical melting patterns confirms that the present model accurately captures the transient phase-change behavior, heat transfer, and evolution of the solid-liquid interface in geometries containing multiple internal heat-transfer tubes.

5. Mesh analysis

A systematic mesh sensitivity analysis was performed before the main calculations. The computational domain was discretized employing a structured quadrilateral grid, with an average skewness of approximately 0.29. In Fig. 3a, three different mesh densities consisting of 90,121, 238968, and 335,950 elements were examined to evaluate the grid dependency of the numerical solution. As observed, the liquid fraction profiles for the three mesh configurations exhibit very similar trends throughout the melting process. Although the coarsest mesh slightly deviates from the other cases at later stages of melting, the results obtained with 238,968 and 335,950 elements are nearly indistinguishable.

This behavior indicates that additional mesh refinement exerts an insignificant effect on the predicted melting behavior. Given the trade-off between computational accuracy and cost, the grid consisting of 238,968 elements was chosen for the present simulations. In addition to the spatial discretization study, a time-step sensitivity analysis was performed to check the accuracy of the transient simulations. In Fig. 3b, the liquid fractions obtained with 0.1 s and 0.05 s show nearly identical outcomes throughout the melting period, whereas a slightly larger deviation is observed with 0.5 s, particularly at intermediate melting stages. This indicates that smaller time steps provide improved resolution of the phase change process. However, the difference between the two mentioned smaller time steps is insignificant, whereas the computational time for the smaller step is significantly higher. Accordingly, the analysis was performed using a time step of 0.1 s.

6. Development of the MLP-based prediction model for stored energy

Accurate prediction of the total stored energy at different melting stages is essential for rapid design assessment and optimization of energy storage systems [54]. While high-fidelity numerical simulations provide detailed thermo-fluidic information, they are computationally intensive, particularly when multiple geometric parameters are varied simultaneously [55]. Therefore, the development of a reliable prediction model capable of estimating system responses in a fraction of computational time becomes highly valuable. Here, a predictive model is proposed to estimate:

- The total stored energy at 9000 s (corresponding to half of the melting process), denoted as E_{half}.
- The total stored energy at 18,000 s (corresponding to complete melting), denoted as E_{full}.

To achieve this objective, a Multilayer Perceptron (MLP) artificial neural network is employed. MLPs are feedforward neural networks composed of an input layer, one or more hidden layers, and an output layer. They are widely utilized in nonlinear regression problems due to their strong ability to approximate complex multidimensional relationships. An MLP learns the mapping between input variables and output responses by adjusting connection weights and biases through iterative training. The presented MLP model includes three geometric parameters as inputs:

- Inner HTF channel' height (CH)
- Inner HTF channel's space between inlet and outlet (CS)
- Angle of the inner HTF channel with respect to the horizontal direction (θ)

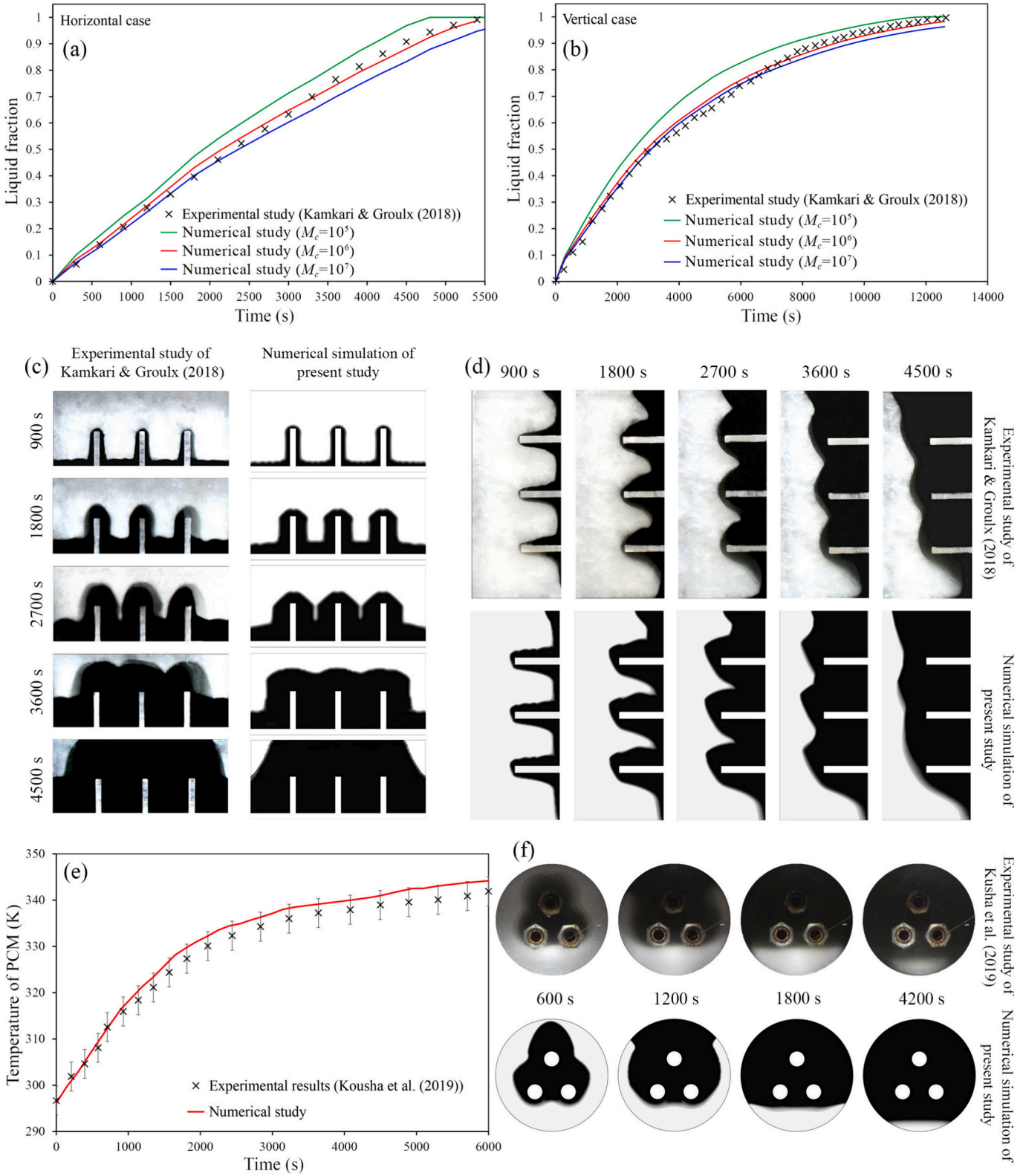

Fig. 2. Comparison of the predicted liquid fraction with the experimental measurements of Kamkari and Groulx [52] for (a) horizontal and (b) vertical rectangular PCM enclosures using three different mushy zone constants (10^5, 10^6, and 10^7). Comparison of the predicted melting fronts with the corresponding experimental observations for the rectangular enclosure in the (c) horizontal and (d) vertical configurations. (e) Comparison of the average PCM temperature predicted by the present model with the experimental results of Kousha et al. [53] for a circular enclosure containing three heated tubes. (f) Comparison of the experimentally observed and numerically predicted melting patterns for the circular enclosure at different charging times.

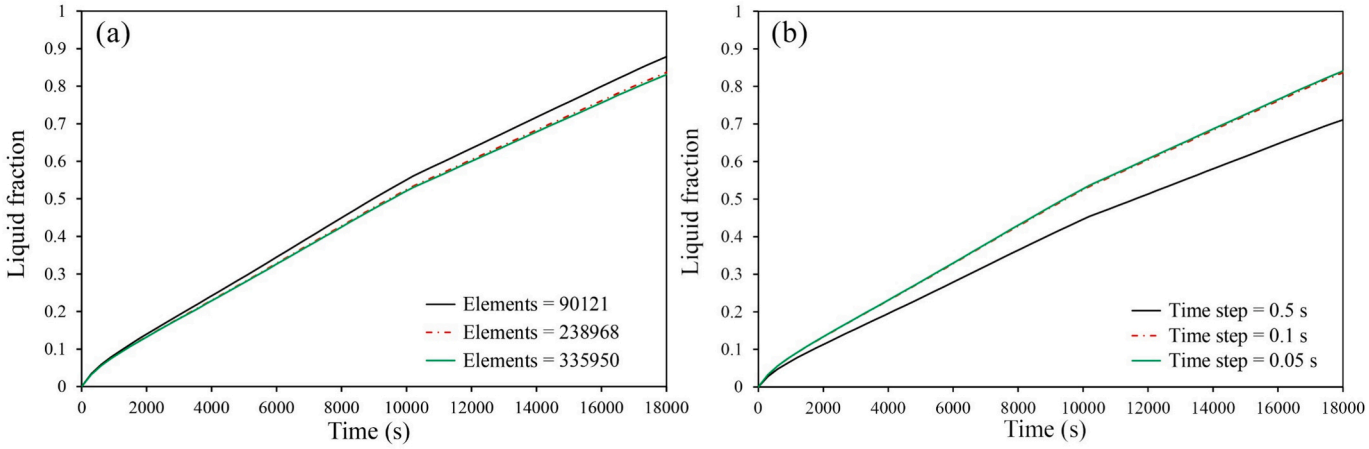

Fig. 3. Impact of (a) grid elements and (b) time step size on the transient variation of the liquid fraction.

These variables are explicitly shown in Fig. 4a. Table 2 presents the three input variables along with the three levels considered for each parameter. The variation levels were selected to systematically investigate the influence of inner HTF channel geometry on energy storage performance. Each variable was assigned three levels:

- Low level (−1)
- Medium level (0)
- High level (+1)

These coded levels correspond to the actual dimensional values of *CH*, *CS*, and θ used in the numerical simulations. Before training the MLP model, all input parameters were normalized. Normalization is a crucial preprocessing step in neural network modeling, ensuring that all input variables contribute proportionally during training. Since *CH*, *CS*, and θ have different physical units and numerical ranges (mm and degrees), using raw values directly may bias the training process toward variables with larger magnitudes. In this study, the inputs were scaled within a standardized range corresponding to the coded levels (−1 to +1). This transformation improves numerical stability, accelerates convergence, and enhances prediction accuracy.

Table 2
Inputs and their variation levels used for developing the MLP prediction model.

Variable	Levels		
	−1	0	+1
CH (mm)	150	215	280
CS (mm)	100	130	160
θ (degree)	80	90	100

The available dataset, obtained from numerical simulations of different geometric states, was randomly divided into three subsets:

- 70% for training
- 15% for validation
- 15% for testing

This division ensures both efficient learning and robust generalization capability. The training set is utilized to update network weights, the validation set prevents overfitting by monitoring generalization error, and the testing set evaluates the final predictive performance. The MLP was constructed and trained in MATLAB using the feedforwardnet tool. To optimize the training phase, the Levenberg–Marquardt algorithm was adopted. Fig. 4b presents the schematic structure of a single neuron in the network. Each neuron performs the following operations:

- Multiplies each input I_i by a corresponding weight W_i.
- Sums the weighted inputs.
- Adds a bias term *b*.
- Passes the result through an activation function *f*.

In the developed MLP model, the nonlinear mapping between geometric parameters and stored energy responses is achieved by appropriately selecting activation functions. The hidden layers apply the hyperbolic tangent sigmoid activation function. The tansig function maps the input signal into the range (−1, +1), introducing strong nonlinearity and improving the network's ability to capture complex interactions among *CH*, *CS*, and θ. Since the inputs were normalized within the same range, the tansig function provides numerical consistency and accelerates convergence during training. For the output layer, the purelin activation function is adopted. Because the network's objective is regression (predicting continuous energy values), a linear activation function ensures that the predicted responses are not

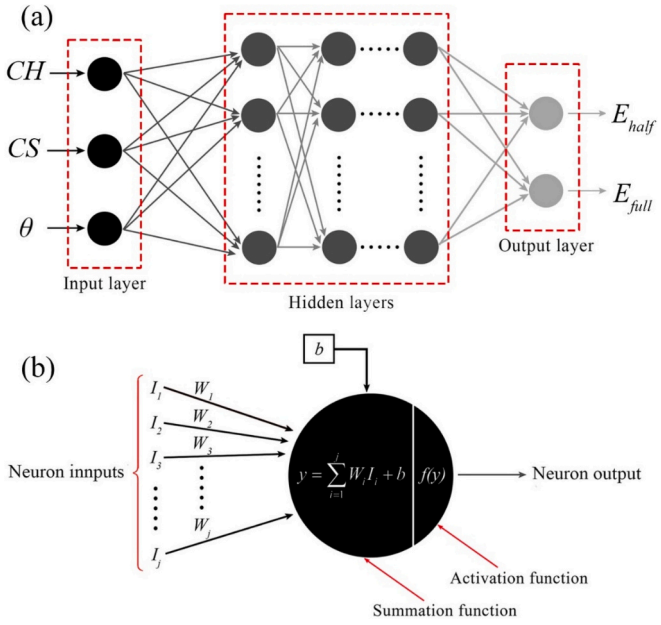

Fig. 4. (a) Structure of the proposed MLP model showing the input layer (CH, CS, θ), hidden layers, and output layer (E_{half}, E_{full}); (b) Schematic representation of a single artificial neuron including weighted inputs, bias term, summation function, and activation function.

artificially bounded and can accurately represent the full range of E_{half} and E_{full}. During training, the network weights and biases are iteratively updated to lessen the loss function, typically defined based on the root mean square error (RMSE) between predicted and numerical simulation values. The quality of the developed model is evaluated using the coefficient of determination (R^2). The training process is repeated until:

- The loss function reaches a minimum value.
- Validation error stabilizes.
- High R^2 values are achieved across the training, validation, and test datasets.

After satisfying these criteria, the final MLP model is obtained and can be used reliably to rapidly predict E_{half} and E_{full} without conducting additional transient simulations.

7. Response surface methodology (RSM) modeling

RSM is a statistical and mathematical technique used to develop predictive models and investigate the relationships between multiple input variables and one or more output responses. RSM approximates the system behavior by fitting a regression equation to the available data, allowing the prediction of responses within the investigated design space. In engineering optimization studies, RSM is widely employed to identify significant factors, evaluate interaction effects between variables, and estimate optimal operating or geometric conditions with considerably lower computational cost than repeated numerical simulations. In the present study, RSM is introduced to further verify the robustness and reliability of the proposed predictive methodology. A quadratic regression model was developed using the same input and output parameters employed in the ANN model (*CH*, *CS*, and θ) as inputs, and the stored energy responses at 9000 s and 18,000 s as outputs. Using identical variables enables a direct and fair comparison between the ANN and RSM approaches. The general second-order RSM equation used in this work is expressed as:

$$Y = \beta_0 + \sum_{i=1}^{k} \beta_i X_i + \sum_{i=1}^{k} \beta_{ii} X_i^2 + \sum_{i<j}^{k} \beta_{ij} X_i X_j + \varepsilon \tag{18}$$

where, Y is the predicted response (E_{half} and E_{full}). x_i and x_j are the coded input variables, β_0 is the intercept term, β_i represents the coefficients of the linear terms, β_{ii} denotes the coefficients of the quadratic terms, and β_{ij} corresponds to the interaction coefficients between variables. The linear terms describe the individual effect of each parameter, the quadratic terms account for curvature in the response surface, and the interaction terms represent the combined influence of two variables on the response. The RSM models were constructed using Design-Expert software based on the full factorial design employed in the numerical simulations. This approach ensures consistency between the numerical dataset, the ANN model, and the RSM model.

8. Optimization strategy for maximizing stored energy

Although the trained MLP and RSM models enable rapid prediction of system responses, identifying the best geometric configuration among countless possible combinations remains a complex task. Exhaustive numerical simulations for all possible parameter combinations would be computationally prohibitive [56]. Therefore, integrating the predictive model with an optimization algorithm provides a powerful and time-efficient solution. Here, a GA is employed to specify the optimal geometric parameters of the inner HTF channel. GAs are population-based evolutionary algorithms inspired by natural selection. They are particularly suitable for nonlinear, multimodal optimization problems where gradient-based methods may fail. The present optimization process is conducted in two stages:

- Single-objective optimization

In the first stage, two independent single-objective optimization problems are solved: the maximization of E_{half} (stored energy at 9000 s) and the maximization of E_{full} (stored energy at 18,000 s). Each objective is optimized separately to identify the geometric configuration that yields the highest performance at the respective melting stage. This approach provides insight into whether optimal designs for half-melting and full-melting conditions coincide or differ, which is important for application-specific design strategies.

- Multi-objective optimization

Then, a multi-objective optimization is performed in which both E_{half} and E_{full} are simultaneously maximized. Unlike single-objective optimization, multi-objective optimization does not yield a single optimal solution but rather a set of Pareto-optimal solutions. These Pareto solutions represent optimal trade-offs where improvement in one objective cannot be achieved without compromising the other. This approach provides designers with a spectrum of high-performance configurations, enabling informed decision-making based on operational priorities.

In the present GA optimization, selected parameters were:

- Population size: 1000. This allows broad exploration of the design space in each generation.
- Generations: 300. This provides sufficient evolutionary iterations for convergence while remaining computationally practical.
- Elite count: 50. This ensures that the top-performing individuals are directly transferred to the next generation, preserving high-quality solutions and accelerating convergence.
- Mutation rate: 0.01. This introduces controlled randomness, preventing stagnation in local optima and maintaining genetic diversity within the population.
- Crossover rate: 0.8. This promotes strong genetic recombination, enabling effective mixing of high-performing traits among individuals.
- Selection method: Stochastic uniform. This method ensures fair probabilistic selection of individuals based on fitness, balancing exploration of new regions and exploitation of promising areas in the search space.

9. Multi-criteria decision making using TOPSIS

While multi-objective optimization presents a Pareto front of optimal solutions, choosing a single final design from the set of non-dominated solutions needs a systematic decision-making approach [57]. Here, the Technique for Order Preference by Similarity to Ideal Solution (TOPSIS) is utilized to rank the Pareto-optimal configurations and identify the most balanced design. In the TOPSIS, the optimal alternative should have:

- The shortest distance from the ideal solution (best possible performance)
- The farthest distance from the anti-ideal solution (worst possible performance)

In the present work, the criteria correspond to the objective functions (E_{half} and E_{full}), and each Pareto solution is treated as an alternative. The mathematical formulation of TOPSIS used in this study is presented in Eqs. (19)–(25), which are explained below. Eq. (19) shows the normalization of the decision matrix [58]:

$$r_{ij} = \frac{x_{ij}}{\sqrt{\sum_{i=1}^{m} x_{ij}^2}} \tag{19}$$

Since different criteria may have different units and magnitudes, normalization is required to eliminate dimensional inconsistencies. The denominator corresponds to the Euclidean norm of criterion j. This step transforms the original decision matrix into a dimensionless normalized matrix r_{ij}, ensuring fair comparison among criteria. Eq. (20) indicates the construction of the weighted normalized matrix [59]:

$$v_{ij} = w_j \cdot r_{ij} \tag{20}$$

Here, w_j denotes the weight assigned to criterion j, reflecting its relative importance. In multi-objective energy storage evaluation, weights may be assigned equally or based on engineering priorities. Multiplying the normalized matrix by the weights produces the weighted normalized matrix v_{ij}, which incorporates both performance values and criterion importance. Eqs. (21) and (22) demonstrate the determination of the ideal and anti-ideal solutions [60]:

$$x_j^{ideal} = \max\{v_{ij}\} \tag{21}$$

$$x_j^{anti-ideal} = \min\{v_{ij}\} \tag{22}$$

Since both E_{half} and E_{full} are beneficial criteria (to be maximized), the ideal value for each criterion is the maximum weighted normalized value across all alternatives. Eqs. (23) and (24) depict the distance from the ideal and anti-ideal solutions [61]:

$$D_i^{ideal} = \sqrt{\sum_{j=1}^{m} w_j \left(x_{ij} - x_j^{ideal}\right)^2} \tag{23}$$

$$D_i^{anti-ideal} = \sqrt{\sum_{j=1}^{m} w_j \left(x_{ij} - x_j^{anti-ideal}\right)^2} \tag{24}$$

Eq. (23) calculates the Euclidean distance between the i^{th} alternative and the ideal solution. A smaller value of D_i^{ideal} indicates that the alternative is closer to the best possible performance. This step quantifies the extent to which each design deviates from the optimal performance boundary. Similarly, Eq. (24) computes the Euclidean distance between the i^{th} alternative and the anti-ideal solution. A larger value of $D_i^{anti-ideal}$ is desirable, as it indicates that the alternative is far from the worst-case scenario. Eq. (25) illustrates the calculation of the closeness coefficient [62]:

$$CC = \frac{D_i^{ideal}}{D_i^{ideal} + D_i^{anti-ideal}} \tag{25}$$

The closeness coefficient determines the relative ranking of each alternative. It combines both distances into a single scalar metric. In practice, the preferred alternative is the one with the highest closeness coefficient.

10. Results and discussion

10.1. Comparative performance of full-factorial designs and the core configuration

Table 3 presents the results of 27 geometrical configurations obtained using the full-factorial design method, along with the core design. The full factorial approach was implemented considering three independent design variables, namely the inner HTF channel height (*CH*), the spacing between the inlet and outlet of the inner HTF channel (*CS*), and the channel inclination angle (θ). Each parameter was examined at three levels of variation. Therefore, the total number of distinct configurations is $3^3 = 27$. This systematic methodology guarantees comprehensive coverage of the design space and enables clear evaluation of the individual and combined effects of the variables on the system's melting and energy-absorption behavior. The core design corresponds to the baseline configuration, in which only the outer HTF channel surrounds the PCM enclosure, with no inner HTF channel. In

Table 3
Geometrical parameters, liquid fraction, total stored energy, pumping power, and thermal–hydraulic performance index (stored energy per unit pumping power) for all investigated designs.

Design number	Variables			Liquid fraction		Total stored energy (kJ)		Pumping power for flow in units (J)		Stored energy per pumping power	
	CH (mm)	*CS* (mm)	θ (degree)	9000 s (2.5 h)	18,000 s (5 h)	9000 s (2.5 h)	18,000 s (5 h)	9000 s (2.5 h)	18,000 s (5 h)	9000 s (2.5 h)	18,000 s (5 h)
1	150	100	80	0.4777	0.8368	7339	11,693	20.4002	40.8003	359,751	286,591
2	150	160	80	0.5315	0.9254	7882	12,499	20.3319	40.6637	387,667	307,375
3	150	100	100	0.5339	0.9275	7922	12,514	20.4151	40.8301	388,046	306,490
4	150	130	80	0.5191	0.9144	7791	12,418	20.1570	40.3140	386,516	308,032
5	150	100	90	0.5195	0.8971	7799	12,209	19.4922	38.9843	400,109	313,177
6	150	130	90	0.5305	0.9244	7883	12,497	19.5922	39.1845	402,354	318,927
7	150	130	100	0.5448	0.9279	8009	12,506	20.5994	41.1989	388,798	303,552
8	150	160	90	0.5474	0.9305	8010	12,510	19.7450	39.4900	405,672	316,789
9	150	160	100	0.5511	0.9243	8040	12,391	20.7003	41.4006	388,400	299,295
10	215	130	90	0.6184	0.9833	8774	13,197	20.9251	41.8502	419,305	315,339
11	215	130	80	0.5835	1	8526	13,524	21.5819	43.1638	395,053	313,318
12	215	160	80	0.6005	0.9791	8619	13,170	21.6148	43.2296	398,755	304,652
13	215	100	90	0.6007	1	8684	13,517	20.8484	41.6968	416,531	324,174
14	215	100	100	0.6339	0.9909	8914	13,254	21.8428	43.6856	408,098	303,395
15	215	100	80	0.5584	0.9540	8285	12,897	21.7329	43.4658	381,219	296,716
16	215	130	100	0.6440	0.9389	8888	12,598	21.9431	43.8863	405,048	287,060
17	215	160	90	0.6280	0.9275	8734	12,492	21.0082	42.0163	415,742	297,313
18	215	160	100	0.6143	0.8826	8485	11,898	22.0570	44.1140	384,685	269,710
19	280	160	100	0.5443	0.7293	7506	9733	23.3110	46.6220	321,994	208,764
20	280	100	80	0.6183	0.9898	8772	13,018	31.5272	63.0543	278,236	206,457
21	280	130	100	0.6311	0.8160	8598	10,783	23.2019	46.4038	370,573	232,373
22	280	130	90	0.6852	0.9216	9306	12,097	22.2433	44.4865	418,373	271,925
23	280	100	100	0.6884	0.9005	9276	11,792	23.1260	46.2520	401,107	254,951
24	280	100	90	0.6797	0.9986	9350	13,035	22.1094	44.2188	422,897	294,784
25	280	160	80	0.6764	0.9477	9269	12,454	22.8187	45.6374	406,202	272,890
26	280	130	80	0.6522	1	9108	13,195	23.0208	46.0416	395,642	286,589
27	280	160	90	0.6459	0.8275	8833	10,993	22.3503	44.7005	395,207	245,926
Core-Design	–	–	–	0.1998	0.3745	3818	6457	11.9685	23.9370	319,004	269,750

this configuration, heat transfer occurs exclusively from the outer boundary toward the center of the PCM domain. Consequently, thermal penetration is limited by the conduction-dominated region in the PCM's core, which restricts melting progression and the rate of stored energy.

To evaluate both transient and final melting behaviors, the liquid fraction and total stored energy are reported at two different time instances: 9000 s (representing half of charging) and 18,000 s (representing the final stage of charging). This dual-time evaluation allows assessment of both intermediate heat absorption dynamics and ultimate storage capacity. The results clearly indicate substantial variation among the 27 modified designs, confirming that *CH*, *CS*, and θ significantly influence the melting process. At 9000 s, the liquid fraction across the 27 designs ranges from 0.4777 (Design 1) to 0.6852 (Design 22). In contrast, the core design reaches only 0.1998 at the same time. This large gap demonstrates the pronounced effect of incorporating the internal HTF channel, even at early melting stages. The presence of two parallel thermal fronts, originating from both the outer and inner HTF channels, substantially promotes heat penetration into the PCM region. At 18,000 s, the superiority of the modified designs becomes even more evident. The liquid fraction among the 27 designs ranges from 0.7293 (Design 19) to complete melting (liquid fraction = 1) in Designs 11, 13, and 26. Meanwhile, the core design achieves only 0.3745 at 18,000 s, indicating that a considerable portion of PCM remains unmolten. Compared to the core design, Designs 11, 13, and 26 exhibit approximately 167% improvement in liquid fraction at 18,000 s. Even the weakest modified configuration (Design 19) still achieves nearly 95% higher liquid fraction than the core design. These findings confirm that all 27 selected configurations are truly influential and meaningfully alter the system's melting characteristics. At 9000 s, the stored energy of the 27 designs ranges between 7339 kJ (Design 1) and 9350 kJ (Design 24), while the core design stores only 3818 kJ. According to Table 3, the total stored energy of the 27 proposed designs at 18,000 s varies significantly, ranging from 9733 kJ in Design 19 to 13,524 kJ in Design 11. In contrast, the core design stores only 6457 kJ. This clearly demonstrates the substantial improvement achieved through geometric modification and parameter optimization. For Design 11, which exhibits the highest stored energy, the enhancement compared to the core design is approximately 109.5%. Even Design 19, which shows the weakest overall melting performance among the optimized cases (in terms of final liquid fraction trend), still stores about 50.7% more energy than the core configuration. This confirms that all modified designs outperform the base model, even the least effective one.

Table 3 also presents the hydraulic performance of all investigated designs, including the pumping power and the thermal–hydraulic performance index (stored energy per unit pumping power). The results indicate that the required pumping power over a 5-h charging period is relatively small, on the order of tens of joules (40 J), which is attributed to the low flow rates, smooth channel geometry, and relatively small pressure gradients within each unit. The simulations show that the pressure drop within an individual unit is approximately 2 Pa, confirming that the longitudinal hydraulic resistance is minimal. However, when the complete multi-unit system is considered, the total pressure drop increases due to local losses at the inlet and outlet of each unit, where the flow is distributed from the main manifold into multiple channels. These values are directly extracted from the CFD simulations. It is noted that these results are also consistent with the predictions of the Darcy–Weisbach equation, confirming the validity of the numerical approach. Among the investigated designs, Design 20 exhibits the highest pumping power demand. This is attributed to its geometric configuration, where a smaller channel spacing (*CS*), larger channel height (*CH*), and lower inclination angle (θ) lead to a sharper inner channel geometry, increasing local flow resistance and thus the pressure drop. The thermal–hydraulic performance index, defined as the ratio of stored energy to pumping power, provides a dimensionless measure for evaluating overall system efficiency. A higher value of this parameter indicates superior combined thermal and hydraulic performance. For the core design, this value is 319,004 at 9000 s, which serves as a baseline reference. Most of the proposed designs outperform the core configuration, except for Design 20, which shows a relatively lower value. The maximum value at 9000 s is obtained for Design 24 (422897), indicating the best overall performance under combined thermal–hydraulic criteria.

At 18,000 s, the core design exhibits a value of 269,750, while most proposed configurations again show higher values, confirming their improved overall performance. The maximum value at this time is achieved by Design 13 (324174). It is also important to note that, since the channels are arranged in parallel, the pressure drop within each individual unit remains nearly identical across all configurations. The pumping power values reported in Table 3 correspond to the total system consisting of all 60 units. The local pressure losses between units were not considered herein, as they remain nearly constant across all designs and would not affect the comparative analysis. However, these effects are explicitly considered in the later 3D simulations (Section 10.4), where inter-unit flow distribution and local losses are fully resolved. Finally, since the longitudinal pressure drop is nearly constant across all configurations and the overall structural layout is identical, it can be concluded that the local pressure loss contribution does not significantly vary among the 27 investigated designs. Therefore, the focus of Table 3 is placed on the variations in longitudinal pressure drop resulting from geometric modifications of the channels, ensuring a clear comparison of design-dependent hydraulic behavior.

To more precisely evaluate the effect of each input variable on system performance, six representative designs out of the 27 cases are selected and analyzed in detail.

- Design 1 represents the baseline experimental configuration in which all input variables are set at level − 1.
- Design 10 corresponds to the mid-level configuration, in which all inputs are set to level 0.
- Design 19 represents the extreme configuration in which all input variables are simultaneously set at level + 1.
- Design 2 is similar to Design 1 (all parameters at level − 1), except that *CS* is increased to level + 1. This isolates the influence of *CS*.
- Design 3 also follows Design 1 except that θ is increased to level + 1, allowing investigation of the angular effect independently.
- Design 20 again follows Design 1, but *CH* is increased to level + 1, highlighting the influence of inner channel height.

These six cases allow a systematic understanding of how each variable modifies the heat transfer and melting performance of the PCM enclosure. At first glance, Fig. 5a clearly shows that the difference in melting performance between the selected configurations and the core design is highly significant. The optimized geometries melt substantially faster than the core configuration. Furthermore, the differences among the six selected designs are also very noticeable. This confirms that each geometric parameter (*CS*, *CH*, and θ) plays a key and influential role in determining the melting behavior. Among the designs, Design 19 initially exhibits the highest liquid fraction and the steepest slope. This indicates very rapid melting at the beginning of the charging process. However, after a certain period, its slope decreases, and its liquid fraction growth weakens relative to other designs. This behavior is attributed to the geometric configuration of the inner HTF channel, where all parameters are at their maximum values. Due to higher *CH*, *CS*, and θ, the inner channel leans strongly toward the outer HTF channel surrounding the PCM enclosure. Consequently, in the upper and lateral sections of the enclosure, the two channels become very close to each other, leaving only a thin PCM layer between them. At the initial stage, this small PCM thickness enables very rapid heat transfer from the HTF to the PCM, accelerating the onset of phase change and producing a steep initial slope in the liquid fraction curve. However, because the inner channel is located near the outer channel, the PCM enclosure's central region suffers from a heat-penetration limitation. Thermal

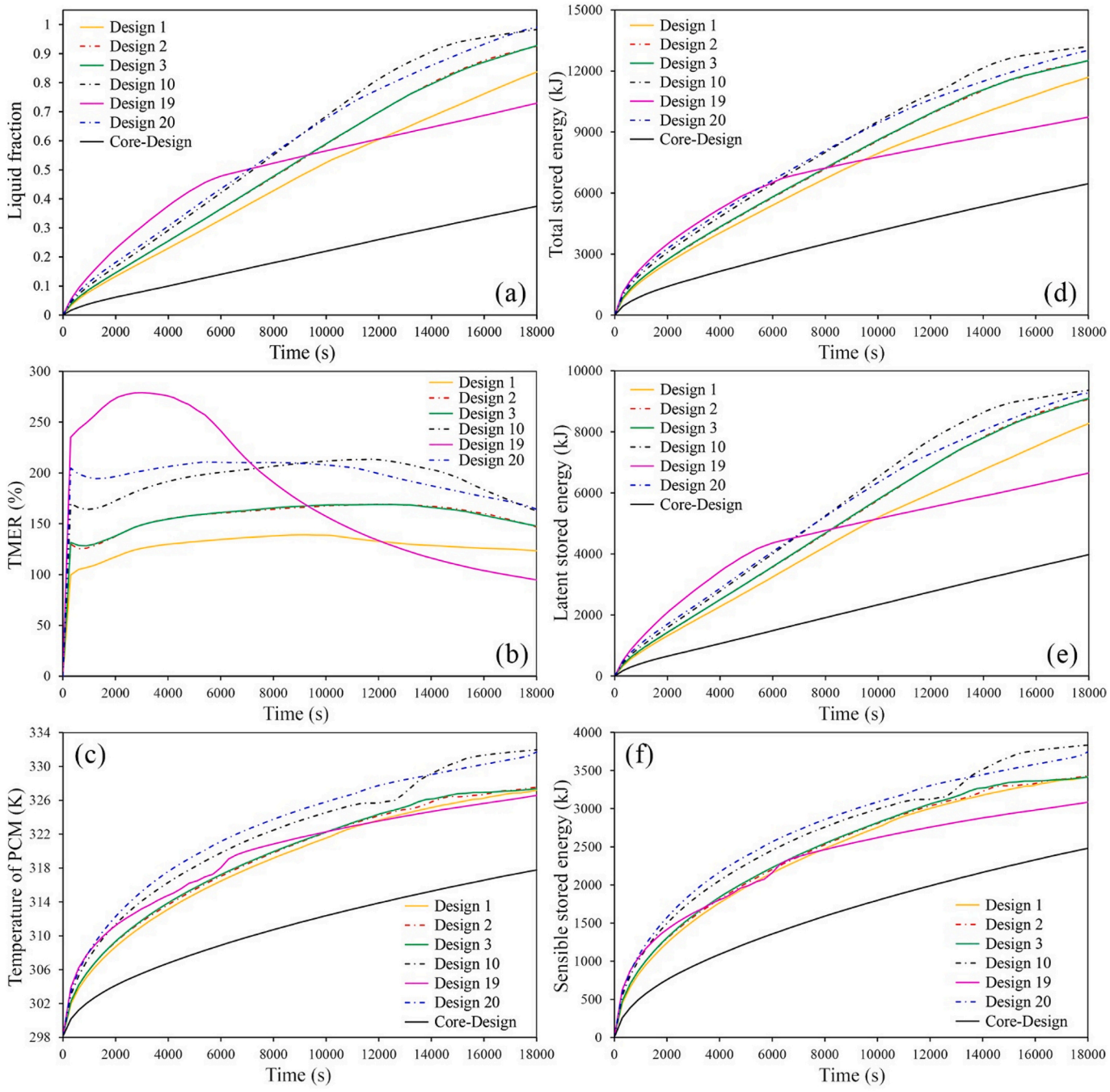

Fig. 5. Time evolution of melting and energy storage characteristics for selected designs compared with the core design.

energy has difficulty reaching the PCM's core. Hence, melting in the central region slows down, and the slope of the liquid fraction curve decreases at later times. Designs 10 and 20 demonstrate more balanced and sustained melting performances. In Design 10, where all variables are at their middle levels, the spacing between the inner and outer channels is appropriate. The channels are well distributed and effectively cover the PCM enclosure's sensitive thermal regions. This leads to a more uniform heat distribution and a consistently high melting rate throughout the process. In Design 20, θ is at its minimum level, causing the inner channel to shift toward the center of the enclosure. Meanwhile, the higher *CH* value enlarges the inner channel and allows it to extend toward the upper sections. This configuration improves coverage of both the central and upper PCM regions, resulting in strong, stable melting performance.

In Fig. 5b, a *TMER* value above 0 indicates performance improvement relative to the base configuration. For example, Design 19 reaches a *TMER* value of approximately 279% at around 3000 s. This indicates that, at that specific moment, its melting performance exceeds that of the baseline design by 279%. However, after this peak, the slope of the *TMER* curve decreases significantly and eventually falls below the values of the other designs. This again reflects the early rapid melting followed by weakened heat penetration in the central PCM region. In contrast, the other selected designs maintain *TMER* values consistently above 0 throughout the entire 18,000 s charging period. Moreover, their slopes remain relatively stable, indicating sustained charging performance compared to the core design.

In Fig. 5c, the PCM temperature in all selected configurations increases more rapidly than in the core design. This confirms that the

geometric modifications significantly enhance heat transfer from the HTF to the PCM. Design 19 shows the steepest temperature rise during the early stages of charging. This is physically consistent with its configuration, in which all geometric parameters are at their maximum values. In this arrangement, the inner HTF channel leans strongly toward the outer channel, reducing the PCM thickness in the upper and side regions. The shorter conduction path enables rapid heat penetration at the start of the charging process, leading to a sharp increase in temperature. However, after the initial period, the slope of Design 19 decreases. The reason lies in the non-uniform thermal distribution created by the channel proximity. Since the inner and outer channels are close to each other, the heat is concentrated near the enclosure boundaries, while the central PCM region becomes thermally shielded. The absence of HTF channels and conductive surfaces in the central parts of the enclosure limits effective heat transfer into the PCM core. As melting progresses, natural convection currents develop due to buoyancy forces. Hot, lighter liquid PCM rises while colder, heavier solid PCM remains in the lower and central regions. In Design 19, the geometry limits effective circulation in the core region, weakening buoyancy-driven convection and slowing the overall temperature rise at later times.

Design 20 exhibits the highest temperature rise during most stages of melting. The balanced geometry (lower θ and higher CH) improves heat penetration into both central and upper PCM regions. Enhanced temperature gradients strengthen natural convection and buoyancy-driven flow, promoting more effective mixing and accelerating melting. At later stages, however, Design 10 slightly surpasses Design 20 in average PCM temperature. Since all variables in Design 10 are at their middle levels, the spacing between channels is optimal, not too concentrated near the walls and not excessively shifted toward the center. This produces a more uniform thermal field, minimizes localized overheating, and allows natural convection to develop efficiently throughout the enclosure. As a result, heat distribution becomes more homogeneous, leading to a slightly higher average temperature toward the completion of the phase-change process. Between approximately 6000 s and 14,000 s, a plateau region is observed in the temperature curves. During melting, a major fraction of the supplied heat is consumed in driving the phase transition instead of increasing the PCM's sensible temperature. Consequently, the temperature rise slows significantly, forming a quasi-plateau behavior. It is important to note that since the reported data in Fig. 5c are related to the average PCM temperature, the curves are not completely flat in this region. While some regions are undergoing phase change at nearly constant temperature, other regions may still be heating sensibly or may have already completed melting and begun sensible heating. The combination of these local variations results in a slightly increasing average temperature during the phase transition interval.

Fig. 5d presents the total stored energy over time. As previously discussed in Table 3, all selected designs absorb significantly more thermal energy than the core design. Design 19 initially stores energy at a very rapid rate, reflected by its steep slope in the early stage. This is again due to the reduced PCM thickness near the upper and side regions, which accelerates initial heat transfer. However, as time progresses, the slope of its energy curve decreases markedly. In fact, during later stages, its energy storage rate becomes comparable to, or even slightly less than, that of the core design. This behavior results from poor heat penetration into the central PCM region and weakened natural convection, which limit further energy absorption. Designs 10 and 20 demonstrate sustained energy storage rates throughout the charging process. By the end of 18,000 s, both designs achieve nearly identical total stored energy, indicating that although their internal heat transfer mechanisms differ slightly, their overall thermal performance is comparable and well-balanced. Fig. 5e shows the latent portion of stored energy. The trends closely follow the melting behavior observed in the liquid fraction curves. All selected designs store substantially more latent energy than the core configuration, confirming enhanced phase change efficiency. Fig. 5f illustrates the sensible energy storage component. During the initial period, the system experiences a rapid rise in sensible heat because the RT50 temperature increases before significant charging begins. Once the phase change dominates, the rate of increase in sensible energy gradually diminishes as an increasing portion of the absorbed heat is redirected into latent heat storage.

10.2. Optimization of the MLP and RSM structures

10.2.1. The MLP model

Accurate prediction of the objective responses is a critical step before performing any optimization procedure. The reliability of the optimization results strongly depends on the predictive capability of the surrogate model. Therefore, identifying the most appropriate structure for the MLP model is essential to ensure both high accuracy and strong generalization ability. An under-parameterized network may fail to capture the nonlinear relationships between inputs and responses, whereas an overly complex network may suffer from overfitting, increased computational cost, and reduced robustness. Consequently, determining the optimal architecture involves balancing model simplicity and predictive performance. In this study, several MLP structures were systematically examined, ranging from the simplest configurations with a limited number of hidden neurons to more complex architectures with larger hidden layers. After extensive testing and comparison of performance metrics, a 3–7–2 structure was selected as the optimal model. This structure consists of three neurons in the input layer (corresponding to the three design variables), seven neurons in a single hidden layer, and two neurons in the output layer (corresponding to E_{half} and E_{full}). The choice of a single hidden layer is consistent with the universal approximation capability of feedforward neural networks, while seven hidden neurons provided sufficient nonlinearity to capture the complex interactions among CS, CH, and θ without introducing unnecessary complexity. Expanding the neuron count beyond seven did not lead to any substantial enhancement in prediction accuracy, whereas reducing the number led to noticeable deterioration in model performance.

Table 4 presents the detailed numerical parameters of the selected MLP model, including the weights and biases of both the hidden and output layers. The hidden layer contains a weight matrix of size (7×3), representing the connection strengths between the three input variables and the seven hidden neurons. Each hidden neuron also includes an associated bias term (7×1), which shifts the activation function and enhances the model's flexibility in fitting nonlinear relationships. In the output layer, two separate sets of weights are reported for predicting E_{half} and E_{full}. Each output neuron receives seven weighted inputs from the hidden layer (7×1), along with a single bias term (1×1). These parameters fully define the trained neural network and enable exact reproduction of the prediction model. The variation in the magnitude and sign of the weights reflects the relative contributions and interactions of each hidden neuron in shaping the final response. Positive and negative coefficients indicate whether a neuron amplifies or counteracts the predicted output. Providing the full set of weights and biases enhances transparency and reproducibility, allowing other researchers to directly implement the developed predictive model without retraining.

10.2.2. The RSM models

Using Design-Expert, the optimal regression equations for E_{half} and E_{full} were derived and are presented in Eqs. (26) and (27), respectively. These equations consist of linear, quadratic, and interaction terms, enabling the models to represent the nonlinear dependency between the configurational variables (CH, CS, and θ) and the thermal performance indicators of the storage system. The inclusion of quadratic and interaction terms improves the ability of the regression models to represent the complex heat transfer and melting behavior observed in the numerical simulations. Consequently, the RSM results provide an additional validation tool for evaluating the accuracy and robustness of the

Table 4
Final weights and biases of the optimized MLP model for predicting E_{half} and E_{full}.

Hidden layer				Output layer			
Weights (7 × 3)			Biases (7 × 1)	Model of E_{half}		Model of E_{full}	
				Weights^T (7 × 1)	Bias (1 × 1)	Weights^T (7 × 1)	Bias (1 × 1)
−1.5740	−0.5869	−0.9732	2.5439	1.6421	−1.1897	0.7994	−0.4497
2.2968	0.2218	0.4154	−2.1204	0.6620		0.0093	
−0.3993	3.1788	−1.1281	1.3793	0.2583		0.2778	
−0.8526	−0.7562	−0.9321	0.6361	−0.2184		0.5075	
2.2365	0.2226	0.1245	2.0957	0.6467		0.4795	
−0.5118	2.1579	−1.4713	1.4752	−0.3850		−0.3519	
−0.3837	0.9567	1.5217	−2.2649	−0.1486		0.1601	

ANN-based predictive framework.

$$E_{half} = -34903.6949 + 83.2221 \times CH + 141.9022 \times CS + 552.0610 \times \theta - 0.1138 \times CH \times CS - 0.3497 \times CH \times \theta - 0.9597 \times CS \times \theta - 0.0674 \times CH^2 - 0.1263 \times CS^2 - 1.9548 \times \theta^2 \quad (26)$$

$$E_{full} = -43735.3932 + 193.9178 \times CH + 199.7320 \times CS + 578.1758 \times \theta - 0.2415 \times CH \times CS - 0.9180 \times CH \times \theta - 1.1263 \times CS \times \theta - 0.1941 \times CH^2 - 0.2199 \times CS^2 - 1.5306 \times \theta^2 \quad (27)$$

10.2.3. The accuracy assessment

To quantitatively evaluate the predictive performance of the developed surrogate models, the statistical indices of the MLP and RSM models are summarized in Table 5. R^2 and RMSE were employed as the primary evaluation metrics, where a higher R^2 and a lower RMSE indicate superior prediction accuracy. For the MLP model, excellent predictive performance was achieved for both responses. The developed network obtained R^2 values of 0.9938 and 0.9939 for E_{half} and E_{full}, respectively, indicating that more than 99.3% of the variation in the numerical results was successfully captured by the proposed neural network. Correspondingly, the RMSE values were only 44.74 kJ for E_{half} and 66.03 kJ for E_{full}, demonstrating that the deviations between the predicted and numerical values were very small throughout the investigated design space. The RSM model also exhibited satisfactory predictive capability. The obtained R^2 values reached 0.9011 for E_{half} and 0.9670 for E_{full}, while the corresponding RMSE values were 179.26 kJ and 153.12 kJ, respectively. These results confirm that the quadratic regression models successfully describe the general relationship between the geometric variables and the stored energy responses. However, their prediction accuracy is noticeably lower than that of the MLP model, particularly for E_{half}. A direct comparison between the two predictive approaches clearly demonstrates the superiority of the MLP model. For both responses, the MLP provides higher coefficients of determination together with substantially lower prediction errors than the RSM model. This improvement originates from the capability of multilayer neural networks to approximate highly nonlinear relationships without being restricted to a predefined quadratic functional form. In contrast, the RSM model is limited to second-order polynomial expressions, which may not completely capture the complex interactions between channel height, channel spacing, channel inclination angle, heat conduction, and natural convection occurring during the melting process. Nevertheless, the RSM model still provides acceptable predictive performance and serves as an independent validation tool, confirming the reliability of the developed ANN framework.

Table 5
Statistical evaluation metrics of the MLP and RSM for E_{half} and E_{full}.

Loss function	Mathematical expression	MLP model		RSM model	
		E_{half}	E_{full}	E_{half}	E_{full}
R^2	$1-\frac{\sum_{i=1}^{m}(r_{num}-r_{pred})^2}{\sum_{i=1}^{m}(r_{num}-\overline{r_{num}})^2}$	0.9938	0.9939	0.9011	0.9670
RMSE	$\sqrt{\frac{\sum_{i=1}^{m}(r_{pred}-r_{num})^2}{m}}$	44.7386	66.0306	179.2577	153.1176

Fig. 6a and b compare the predictions of the developed MLP and RSM models with the corresponding numerical simulation results for the stored energy at 9000 s (E_{half}) and 18,000 s (E_{full}), respectively. In both figures, the solid diagonal line represents perfect agreement between the predicted and numerical values. Therefore, the closer the predicted points are to this line, the higher the prediction accuracy of the corresponding surrogate model. The predictions of the MLP model almost completely overlap the numerical data. In contrast, although the RSM model generally follows the overall trend, the green markers exhibit noticeably larger deviations from the diagonal line, particularly in the low and medium stored-energy regions. These deviations are in agreement with the statistical outcomes depicted in Table 5, where the RSM model achieved a lower R^2 and a considerably larger RMSE than the MLP model. Overall, the MLP model outperforms the RSM model in predicting both E_{half} and E_{full}. The multilayer neural network provides higher prediction accuracy, lower deviation from the numerical simulations, and better capability to capture the nonlinear interactions among the design variables. Consequently, although the RSM model is retained as an independent validation tool to verify the robustness of the proposed predictive methodology, all subsequent analyses, response surface investigations, and optimization studies presented in this work are based solely on the MLP model owing to its superior predictive performance.

Among the 27 full-factorial design cases, 70% of the samples were employed for network training, whereas the remaining 30% were reserved exclusively for validation and testing and were never introduced during the training stage. It is worth emphasizing that the performance metrics reported in Table 5, as well as the comparisons presented in Fig. 6a and b, were evaluated using the entire dataset, including the training, validation, and testing samples, rather than only the training subset. Therefore, the reported R^2 and RMSE values represent the overall predictive capability of the developed models across all available data. The excellent agreement between the MLP predictions and the numerical results over the complete dataset confirms that the proposed model has successfully generalized beyond the training data, accurately predicting not only the samples used for learning but also previously unseen validation and testing cases. This strong generalization capability demonstrates that the MLP model has learned the underlying physical relationships governing the thermal energy storage system instead of merely memorizing the training samples. To further strengthen the reliability of the proposed predictive methodology, six additional geometries outside the original full-factorial dataset were introduced. These new cases were generated systematically by assigning intermediate normalized levels of 0.75, 0.50, 0.25, −0.25, −0.50, and −0.75 to all three design variables, resulting in Designs 28–33. Since none of these geometries were included in the original training, validation, or testing datasets, they provide a rigorous assessment of the extrapolation capability of the developed MLP model. The prediction results for the six

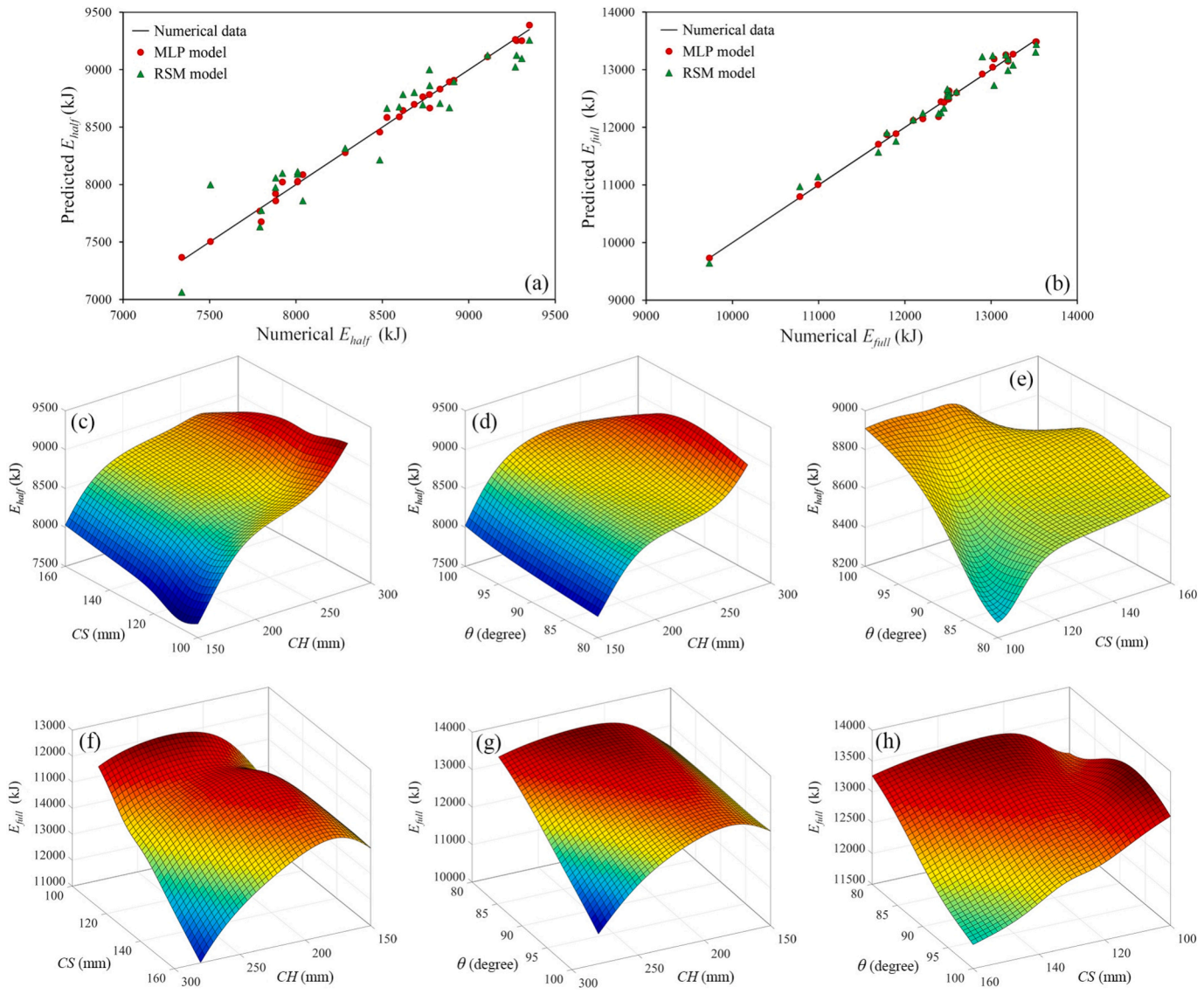

Fig. 6. Validation of the MLP and RSM prediction models, and three-dimensional response surfaces of E_{half} and E_{full} as functions of CS, CH, and θ.

Table 6
Comparison between numerical and MLP-predicted stored energy for six additional unseen geometries.

Design number	Variables			Numerical total stored energy (kJ)		MLP predicted total stored energy (kJ)		Error (%)	
	CH (mm)	*CS* (mm)	*θ* (degree)	E_{half}	E_{full}	E_{half}	E_{full}	E_{half}	E_{full}
28	231.25	137.5	92.5	9084	12,576	8897	12,603	2.06	0.21
29	198.75	122.5	87.5	8506	13,534	8526	13,308	0.24	1.67
30	247.5	145	95	9061	11,773	8804	11,825	2.80	0.44
31	182.5	115	85	8204	13,319	8295	13,077	1.11	1.82
32	263.75	152.5	97.5	8637	10,748	8444	10,782	2.23	0.32
33	166.25	107.5	82.5	7932	12,421	7867	12,459	0.82	0.31

newly generated geometries are presented in Table 6. The numerical simulations are compared directly with the MLP predictions for both E_{half} and E_{full}, together with their corresponding prediction errors. An excellent agreement is observed for all six cases, confirming that the proposed neural network accurately predicts the thermal performance even for geometries that were completely excluded from the model development process. For E_{half}, the prediction errors vary between 0.24% and 2.80%, while for E_{full}, the errors range from only 0.21% to 1.82%. Even the largest prediction error remains below 3%, demonstrating the remarkable prediction capability of the proposed model. Such low deviations confirm that the MLP successfully captures the underlying nonlinear relationships governing the charging process and is not limited to memorizing the original training data.

A k-fold cross-validation strategy is conducted to further verify that the developed MLP models do not suffer from overfitting and that their predictive performance is not dependent on a particular training/testing partition. In the present work, the dataset was divided into 3 folds, where, in each iteration, 18 samples were used for training and the remaining 9 samples were used for testing. This procedure was repeated three times until every sample had been used once for testing. The

obtained results show that R^2 remains greater than 0.98 in every fold and every iteration for both prediction models, demonstrating that the predictive performance is insensitive to the particular training/testing partition and that the model does not suffer from overfitting. Furthermore, cross-validation reduces the influence of random sampling and provides a more reliable assessment of the model's generalization ability. These results confirm that the excellent performance of the proposed MLPs arises from their ability to successfully model the underlying nonlinear dependency between the configurational variables and the thermal responses, rather than simply memorizing the training data.

Figs. 6c–6h illustrate the 3D response surfaces generated by the trained MLP model. These surfaces provide deeper insight into the individual and combined effects of *CS*, *CH*, and θ on the energy storage performance. By observing the curvature, gradients, and color variations of these surfaces, one can identify dominant parameters, interaction effects, and optimal regions within the design space. The surfaces reveal not only linear trends but also nonlinear interactions among variables, highlighting the complex thermal behavior driven by conduction, natural convection, channel geometry, and heat-penetration mechanisms. Fig. 6c shows the variation of E_{half} with *CS* and *CH*. A distinct interaction effect is observed. At lower *CH* values, increasing *CS* enhances E_{half}. In this region, a larger *CS* improves channel spacing, promoting better heat distribution and facilitating earlier melting. However, at higher *CH* values, increasing *CS* reduces E_{half}. In this case, the combined enlargement of both geometric parameters causes thermal imbalance and reduces effective heat penetration in certain PCM regions. In contrast, increasing *CH* consistently enhances E_{half} across all *CS* values. A higher *CH* enlarges the heat transfer surface and improves thermal coverage during the early melting stage (around 9000 s), making *CH* a strongly influential parameter for mid-time energy storage.

Based on Fig. 6d, at lower θ values, increasing *CH* significantly enhances E_{half}. In this configuration, the inner channel is oriented more toward the central region of the PCM enclosure, and enlarging *CH* improves heat penetration and strengthens buoyancy-driven convection. However, at higher θ values, the trend becomes nonlinear: increasing *CH* initially enhances E_{half}, but after reaching a certain point, further increase reduces it. This is due to excessive leaning of the inner channel toward the outer channel, which leads to non-uniform heat distribution and thermal shielding in the core region. Fig. 6e demonstrates that the color gradient across the surface is less pronounced compared to Fig. 6c and d. The smaller variation in the color spectrum indicates that the combined effect of *CS* and θ on E_{half} is weaker than that of *CH*. This observation confirms that *CH* emerges as the dominant factor influencing the amount of stored energy at 9000 s. While *CS* and θ do modify the melting behavior, their impact is secondary compared to the dominant role of channel height in determining mid-stage energy absorption.

Fig. 6f shows the combined influence of *CS* and *CH* on E_{full} (stored energy at 18,000 s). Increasing *CH* initially enhances E_{full}, but beyond an optimal value, further increase causes a reduction. This behavior reflects the balance between improved heat transfer area and potential thermal non-uniformity at excessive channel heights. Increasing *CS* consistently decreases E_{full}, and this decreasing trend becomes more pronounced at higher *CH* values. When both *CS* and *CH* are large, the channel configuration promotes uneven heat penetration and limits effective melting in certain PCM regions during the later stages. In Fig. 6g, increasing *CH* first enhances E_{full}, then decreases it. This nonlinear trend becomes more significant at higher θ values. When θ is large, the inner channel leans toward the outer wall, and excessive *CH* amplifies thermal concentration near the boundaries while weakening heat penetration toward the center. Increasing θ decreases E_{full}, and this effect is stronger at higher *CH* values. A larger θ shifts the inner channel away from the central PCM region, reducing the effectiveness of natural convection circulation in the core and limiting long-term energy storage. Fig. 6h reveals that increasing *CS* decreases E_{full}, and this reduction becomes more pronounced at higher θ values. Similarly, increasing θ decreases E_{full}, and this effect intensifies at higher *CS* values. This mutual amplification of negative effects indicates that excessive spacing combined with excessive inclination results in suboptimal heat distribution within the enclosure. The central PCM region becomes thermally less accessible, reducing the total energy absorbed during the full charging period.

10.3. GA-based optimization of the storage performance

Although the surface plots presented in the previous subsection provide valuable insight into the interaction between design variables and system performance, they are primarily qualitative tools and cannot precisely determine the optimal design parameters. Surface plots primarily illustrate trends and the system's general sensitivity to parameter variations; however, identifying the exact combination of variables that yields the best performance requires an optimization approach. Therefore, a GA is exerted to determine the optimal geometric configuration of the proposed thermal energy storage unit. The objective of the proposed optimization framework is not to search only among the original 27 full-factorial designs. Instead, the CFD simulations are first used to construct a continuous surrogate model (MLP), which approximates the nonlinear relationship between the design variables and the thermal responses over the entire design space. GA is then applied to this continuous response surface, allowing it to evaluate an unlimited number of candidate solutions within the prescribed variable ranges. Therefore, the optimization is not a selection or interpolation between the 27 original designs, but rather a continuous global search over the mathematical model represented by the trained MLP. Table 7 presents the sensitivity analysis of the genetic algorithm by independently varying five major GA parameters, including population size, maximum number of generations, elite count, mutation rate, and crossover rate, by ±10% relative to their default values. The obtained optimal values of E_{half} and E_{full} exhibit negligible variations, with all changes remaining below 0.06%. These results demonstrate that the proposed optimization framework is highly robust and that the identified optimal designs are essentially independent of moderate variations in the GA control parameters.

First, a single-objective optimization strategy is adopted. Two separate optimization objectives are considered to evaluate the storage performance at different stages of the charging process. The first objective is to maximize the stored energy at half charging time, denoted E_{half}, which corresponds to the total energy stored in the PCM at 9000 s. The second objective is to maximize the stored energy at full charging time, denoted E_{full}, corresponding to the stored energy at 18,000 s. By optimizing these two objectives separately, the study aims to identify configurations that either enhance early-stage energy storage capability or maximize the system's total energy storage capacity. The GA-optimized results are presented in Table 8. For maximizing stored energy at 9000 s, the GA proposes a configuration called the Optimal Design for Half-time (*ODH*). According to Table 8, the optimal parameters for *ODH* are $CH = 280$ mm, $CS = 100$ mm, and $\theta = 94.08°$.

Table 7
Sensitivity analysis of the genetic algorithm settings and their effects on the optimized values of E_{half} and E_{full}.

GA setting parameters	Change interval	Response (kJ)		Changes from the default mode (%)	
		Best E_{half}	Best E_{full}	Best E_{half}	Best E_{full}
Population size	+10%	9459	13,540	0.01	0.05
	−10%	9458	13,540	0	0.05
Maximum number of generations	+10%	9459	13,538	0.01	0.04
	−10%	9459	13,540	0.01	0.05
Elite count	+10%	9459	13,540	0.01	0.05
	−10%	9458	13,539	0	0.04
Mutation rate	+10%	9458	13,534	0	0.01
	−10%	9456	13,537	0.02	0.03
Crossover rate	+10%	9457	13,539	0.01	0.04
	−10%	9455	13,533	0.03	0

Table 8
Optimal design variables obtained from GA-based optimizations for E_{half} and E_{full}.

Response	Symbol	Variables		
		CH (mm)	*CS* (mm)	θ (degree)
E_{half}	*ODH*	280	100	94.0800
E_{full}	*ODF*	205.7050	100	93.1800
E_{half} and E_{full}	*ODB*	280	100	88.8704

Similarly, when the optimization objective is shifted to maximize the total stored energy at 18,000 s, the GA identifies another optimal configuration, referred to as the Optimal Design for Full-time (*ODF*). The corresponding optimal geometric parameters for *ODF* are $CH = 205.705$ mm, $CS = 100$ mm, and $\theta = 93.18°$, as presented in Table 6. A comparison between the two optimal designs reveals that the channel spacing remains constant at 100 mm in both cases, suggesting that this spacing offers a favorable balance between heat transfer surface area and PCM volume. However, the channel height and the inclination angle exhibit noticeable variations, highlighting their important roles in controlling heat transfer distribution in the enclosure. The fact that one of the optimal solutions (*ODH*) is located close to Design 24 does not indicate a limitation of the optimization procedure. Instead, it suggests that the global optimum for this particular objective is naturally located near that region of the design space. This behavior is expected in surrogate-based optimization and demonstrates that GA successfully converges toward the region with the highest predicted performance. Moreover, the optimization results are not confined to a single neighborhood. The GA identified three different optimal configurations (*ODH*, *ODF*, and *ODB*) corresponding to different optimization objectives, each possessing distinct geometric parameters and thermal characteristics. This further demonstrates that the optimization framework effectively explores the design space according to the selected objective function rather than simply reproducing one of the original full-factorial designs.

Relying solely on single-objective optimization is not always practical in real engineering applications. In many thermal energy storage systems, improving one performance indicator often comes at the expense of another. For instance, a design that maximizes stored energy at the early stage of charging may not necessarily yield the highest total stored energy at the end of charging. Therefore, to achieve a balanced design that simultaneously considers both performance indicators, a multi-objective optimization procedure is also applied in this study. The results of this optimization are presented in Fig. 7, which illustrates the distribution of solutions generated during the GA search. The yellow markers represent random solutions explored by the GA across the design space. These points demonstrate the wide range of possible combinations of design variables and the corresponding values of E_{half} and E_{full}. As optimization progresses, the algorithm identifies a set of non-dominated solutions, known as the Pareto front, represented by the red markers. These solutions form the optimal trade-off curve between the two objectives, meaning that improving one objective beyond these points would worsen the other.

From the Pareto front, several candidate optimal designs can be observed. The figure also highlights the previously obtained single-objective optimal designs, namely the *ODH* and the *ODF*. The *ODH* design is located toward the right side of the Pareto front, where the value of E_{half} is maximized, whereas the *ODF* design appears toward the upper region, where E_{full} reaches its maximum value. Since all Pareto solutions are optimal from a mathematical perspective, selecting the most practical design among them requires a decision-making technique. Using TOPSIS, the solution that simultaneously maintains high values of both E_{half} and E_{full} is selected as the final optimal design. This configuration is referred to as the Optimal Design for the Balanced state (*ODB*). The corresponding optimal geometric parameters of *ODB* are also listed in Table 8, and the locations of *ODH*, *ODF*, and *ODB* are clearly illustrated in Fig. 7. The design selected using the TOPSIS demonstrates a balanced performance between the two single-objective optimal designs, namely *ODH* and *ODF*. The optimal design identified by TOPSIS has a closeness coefficient of 0.7329 and corresponds to the geometric parameters $CH = 280$ mm, $CS = 100$ mm, and $\theta = 88.8704°$.

To further evaluate the reliability of the developed prediction model, the optimal designs obtained from the optimization process were re-

Table 9
Comparison between MLP-predicted results and numerical simulation results for the optimal designs, including the corresponding prediction errors.

Design symbol	Predicted results (kJ)		Numerical results (kJ)		Error (%)	
	E_{half}	E_{full}	E_{half}	E_{full}	E_{half}	E_{full}
ODH	9458	12,788	9402	12,585	0.5956	1.6130
ODF	8752	13,533	8654	13,544	1.1324	0.0812
ODB	9346	13,248	9287	13,113	0.6353	1.0295

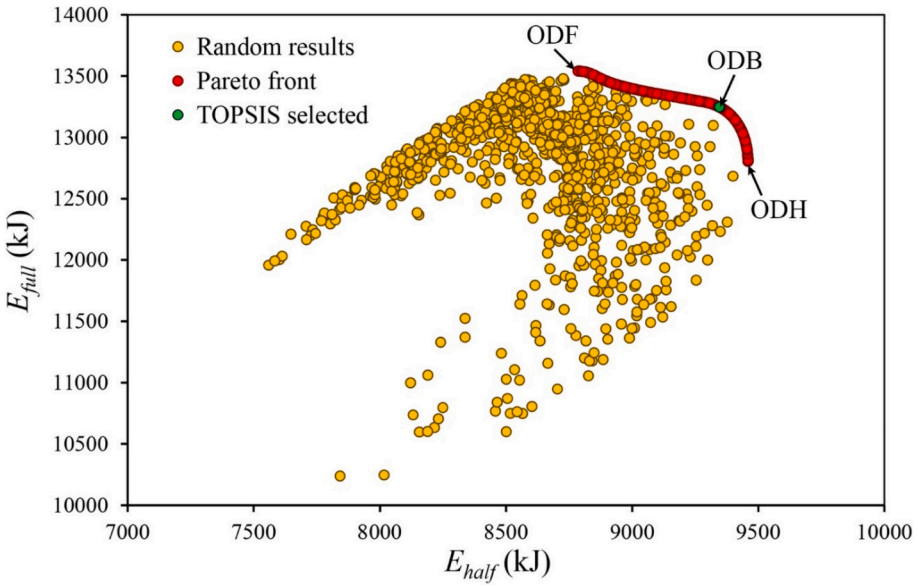

Fig. 7. Pareto front showing the trade-off between E_{half} and E_{full}, including random solutions, Pareto optimal solutions, and the TOPSIS-selected optimal design.

simulated numerically and compared with the MLP-predicted values. The comparison between the anticipated data and the numerical findings is presented in Table 9. The error values for both E_{half} and E_{full} remain very small for all three optimal configurations (*ODH*, *ODF*, and *ODB*). For the *ODH* design, the prediction error is approximately 0.5956% for E_{half} and 1.6130% for E_{full}. Similarly, the *ODF* design exhibits errors of 1.1324% for E_{half} and 0.0812% for E_{full}. For the *ODB*, the prediction errors are 0.6353% for E_{half} and 1.0295% for E_{full}. These very small deviations between the anticipated and numerical findings confirm the high predictive capability and reliability of the MLP model. The close agreement demonstrates that the trained neural network can accurately estimate the system's energy storage performance across different geometric configurations. Consequently, the model can be confidently used as a rapid and reliable tool for design optimization, significantly reducing the computational cost and time required for repeated numerical simulations. From Table 9, it is seen that the performance of *ODB* lies between those of *ODH* and *ODF*, although it remains very close to the *ODH*. Considering both short-term and long-term energy storage performance, *ODB* provides the most balanced and practical solution among the optimal designs. Therefore, this configuration can be regarded as the most suitable design for achieving efficient performance under both early-stage and long-duration charging conditions.

To further verify that the selected time step remains appropriate for the optimized geometry, an additional time-step independence study was carried out for the *ODB*. The time steps of 0.5 s, 0.1 s, and 0.05 s were investigated, and the corresponding liquid fraction histories are compared in Fig. 8. As shown in the figure, the solution obtained with a time step of 0.5 s exhibits a noticeably slower melting process and underestimates the liquid fraction throughout the charging period. In contrast, the predictions obtained using 0.1 s and 0.05 s overlap almost completely over the entire simulation, indicating that further reduction of the time step produces negligible changes in the numerical results. Therefore, temporal independence is achieved with a time step of 0.1 s. Considering that the smaller time step of 0.05 s substantially increases the computational cost without providing any meaningful enhancement in accuracy.

As observed in Fig. 9a, all optimized configurations significantly accelerate the melting process relative to the reference geometry. Among the optimal configurations, the *ODH* initially exhibits the fastest melting rate. However, its advantage gradually diminishes as the charging process progresses. The geometric characteristics of *ODH* can explain this behavior. In this configuration, the channel height is relatively large ($CH = 280$ mm), and the channel angle is $\theta = 94.08^{\circ}$. The larger angle causes the inner HTF channel to move closer to the outer HTF channel, which reduces the effective heat transfer coverage in the central parts of the enclosure. Additionally, the larger channel height brings the inner HTF channel closer to the upper sections of the enclosure, enhancing heat transfer in these regions. As a result, heat transfer in the upper regions becomes dominant while the central regions receive less thermal interaction. Consequently, the melting process starts rapidly due to strong heat transfer near the channels, but as the melting front progresses toward the center, it becomes weaker because of insufficient heat transfer in the middle regions.

The *ODB* demonstrates an intermediate behavior between *ODH* and *ODF*. At the initial and middle stages, its performance is very close to that of *ODH*, while in the final stages, it approaches that of *ODF*. This balanced behavior arises from its geometric parameters. In *ODB*, the channel height remains relatively large ($CH = 280$ mm), which allows the upper regions of the PCM enclosure to be effectively heated. However, the channel angle is smaller ($\theta = 88.8704^{\circ}$), which moves the inner HTF channel slightly toward the central parts of the container. This adjustment improves heat transfer coverage in the middle regions while still maintaining strong heating in the upper sections. As a result, the melting process proceeds efficiently at both the middle and final stages, resulting in a well-balanced thermal performance. Quantitatively, the liquid fraction values at 9000 s are 0.6905 for *ODH*, 0.5990 for *ODF*, and 0.6721 for *ODB*, whereas the core design only reaches 0.1998 at the same time. This corresponds to improvements of approximately 245.6% for *ODH*, 199.8% for *ODF*, and 236.3% for *ODB* compared with the core design. At 18,000 s, the liquid fractions are 0.9649 for *ODH*, 1 for *ODF* and *ODB*, while the core design reaches only 0.3745. These correspond to enhancements of about 157.6% for *ODH*, 167.0% for *ODF*, and 167.0% for *ODB* relative to the reference configuration.

Comparing the optimal designs themselves, the *ODB* configuration achieves a liquid fraction about 12.2% higher than *ODF* at 9000 s, although it remains about 2.7% lower than *ODH* at this time. At the final stage (18,000 s), both *ODB* and *ODF* achieve complete melting, yielding a liquid fraction about 3.6% higher than that of *ODH*. The *TMER* trends in Fig. 9b further clarify the differences between the optimal configurations. At early stages, the *ODH* configuration exhibits the highest TMER (257% at 5700 s), indicating a faster melting rate due to stronger

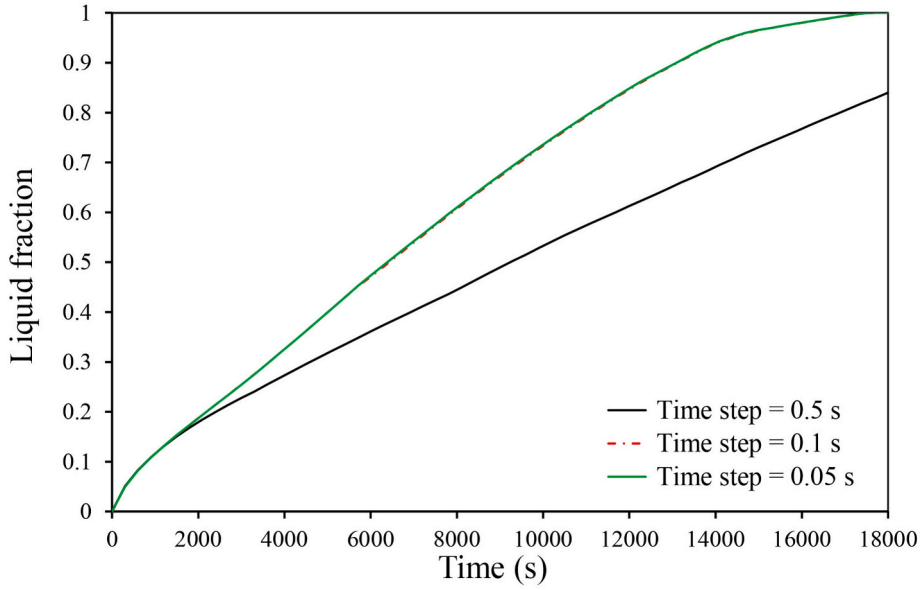

Fig. 8. Time-step independence study for the ODB. Comparison of the predicted liquid fraction histories obtained using three different time steps.

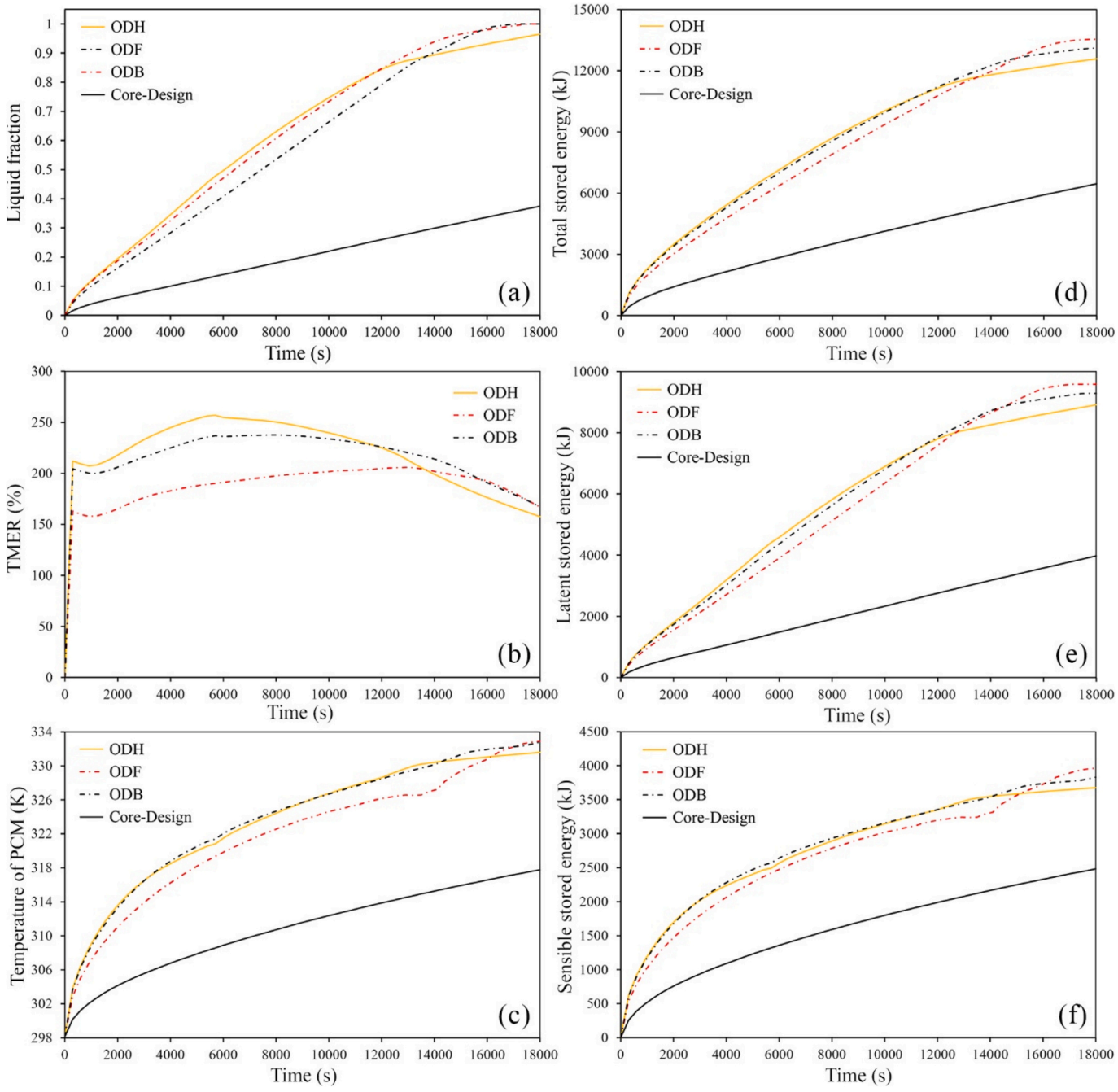

Fig. 9. Time evolution of charging and energy storage behavior for the optimized designs compared with the core design.

heat transfer near the HTF channels. Nevertheless, as the charging process progresses, the advantage of *ODH* gradually decreases due to reduced heat transfer effectiveness in the central region. As a result, the *ODF* configuration eventually surpasses *ODH*, demonstrating a more sustained melting capability toward the end of the charging period. The *ODB* configuration behaves consistently across *ODH* and *ODF*, reflecting its balanced geometric design that simultaneously supports effective early melting and sustained heat transfer during the later stages.

In Fig. 9c, the optimized configurations exhibit significantly faster temperature rise than the reference geometry, due to improved heat transfer surfaces and enhanced HTF–PCM interaction. At the early stages of charging, the *ODH* shows the fastest rate of temperature increase, followed closely by the *ODB*. The *ODF* exhibits a slightly slower rise in the early stages, reaching roughly 323.69 K at 9000 s. However, it can reach the HTF temperature of around 333.15 K (332.88 K) at the end of 18,000 s, whereas the core design only reaches about 317.77 K at this timeframe. A noticeable plateau region appears in all curves approximately between 6000 s and 14,000 s. This plateau corresponds to the phase-change period, during which most of the supplied heat is consumed in driving the phase transition instead of raising the sensible temperature of the material. As a result, the temperature rise temporarily slows down, creating the nearly flat region in the curves. However, the curves are not perfectly flat because the values shown represent the average temperature of the PCM domain. After most of the PCM melts, the temperature begins to rise more noticeably toward the end of the charging.

In Fig. 9d, the differences between the designs become clearer in this figure. At 9000 s, the *ODH* design stores the largest amount of energy, reaching 9402 kJ, followed closely by *ODB* with 9287 kJ, while *ODF* stores 8654 kJ. In comparison, the core design stores only 3818 kJ.

These results demonstrate that the optimized configurations significantly accelerate charging during the first half of operation. Specifically, compared with the core design, the stored energy at 9000 s improves by approximately 146% for *ODH*, 126.6% for *ODF*, and 143.2% for *ODB*. At 18,000 s, the trend begins to change slightly. The *ODF* design becomes the best-performing configuration, storing 13,544 kJ, while *ODB* stores 13,113 kJ and *ODH* stores 12,585 kJ. In contrast, the core design reaches only 6457 kJ, which results in the improvements of about 94.9% for *ODH*, 109.8% for *ODF*, and 103.1% for *ODB*. Comparing the optimized designs themselves, the *ODB* configuration stores about 1.2% less energy than *ODH* at 9000 s but about 7.3% more energy than *ODF*, indicating its balanced short-term performance. At 18,000 s, *ODB* stores approximately 4.2% more energy than *ODH* but about 3.2% less energy than *ODF*, confirming that its performance lies between the two single-objective optimal designs.

It can also be observed that the *ODF* curve eventually reaches the highest total stored energy. This behavior is mainly related to its geometric structure. In the *ODF* configuration, the inner HTF channel height is smaller, which allows a larger volume of PCM to occupy the enclosure. Consequently, a greater mass of PCM participates in the energy storage process, leading to a higher total thermal energy storage capacity by the end of the charging period. Fig. 9e and f present the variations in latent and sensible stored energy, respectively. The trends in these figures are consistent with the overall energy storage behavior observed in Fig. 9d. The latent energy curves mainly reflect the PCM's melting progression and show significant improvements for the optimized designs due to faster phase change. Meanwhile, the sensible energy curves illustrate the temperature-driven energy storage before and after the phase change process. Together, these figures confirm that the optimized geometries enhance both melting performance and total energy storage capability compared with the core design.

The contours in Fig. 10 clearly demonstrate the influence of the inner HTF channel geometry, particularly its height and angle, on the PCM's charging behavior. In all cases, the melting process begins near the HTF channels, where the temperature gradient between the HTF and the solid PCM is highest. Additionally, since the HTF inlet is on the left side of the enclosure, the fluid entering this region has a slightly higher temperature than that at the outlet regions, leading to stronger melting on the left side during all stages of charging. For the *ODH* configuration, the inner HTF channel has a larger height and a larger channel angle. At 3600 s, melting primarily occurs along the outer and inner HTF channel surfaces, forming thin liquid layers around the channels. Because of the higher channel height, the upper regions of the PCM enclosure receive heat earlier, leading to visible melting near the top of the geometry. As the melting progresses to 7200 s and 10,800 s, two elongated melted regions appear along the side walls of the enclosure. The melted PCM in these regions rises due to buoyancy forces, while the colder and denser solid PCM remains in the lower regions. This natural convection circulation enhances heat transfer near the heated walls but leaves a relatively large solid PCM region in the center, since the larger channel angle moves the inner HTF channel closer to the outer channel, reducing direct heat penetration into the central region. Consequently, although *ODH* exhibits rapid initial melting near the channels, a residual solid core remains longer in the middle of the enclosure.

The *ODF* design shows a different melting behavior due to its smaller inner channel height. At 3600 s, the melting region develops around both HTF channels but remains concentrated near the channel walls. Because the inner channel is positioned lower in the enclosure, the upper

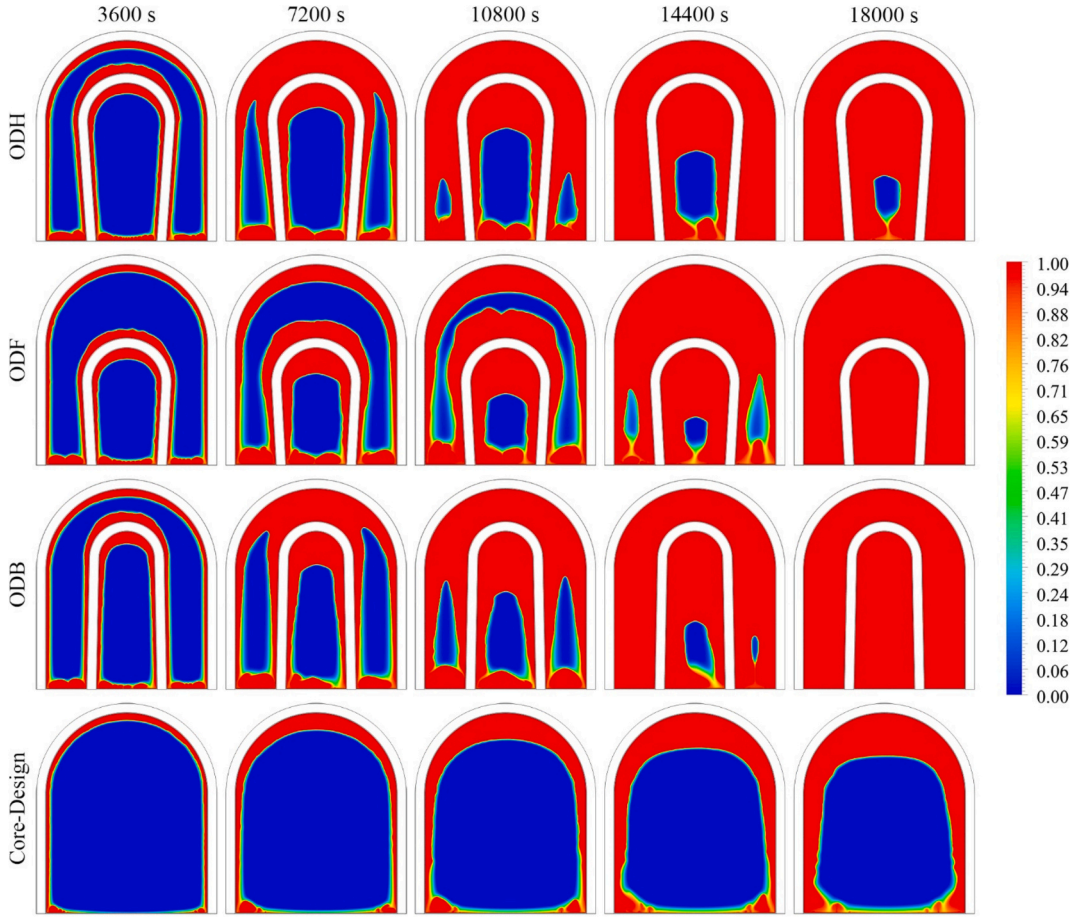

Fig. 10. Liquid fraction contours of the PCM for the optimized designs (*ODH*, *ODF*, and *ODB*) and the core design at different charging times.

regions of PCM initially receive less direct heat transfer. However, as the process continues toward 7200 s and 10,800 s, the melting front expands upward along the outer walls and gradually toward the center. The melted PCM near the heated walls becomes lighter due to its reduced density with increasing temperature, causing it to rise under buoyancy forces, while the cooler PCM sinks under gravity, generating natural convection currents. These convective flows enhance heat transport from the channel surfaces toward the interior regions. As a result, by 14,400 s, most of the PCM has melted except for a small region near the center-bottom. At 18,000 s, the enclosure becomes almost completely melted. The smaller inner channel height in *ODF* allows more PCM volume in the enclosure, which slightly delays the initial melting but results in a more uniform and complete melting process at later stages.

The *ODB* configuration, which represents the balanced optimal design, shows melting characteristics between *ODH* and *ODF*. At 3600 s, the melted regions appear around both the outer and inner HTF channels, similar to *ODH*, due to the relatively large channel height. However, the smaller channel angle moves the inner HTF channel slightly closer to the center of the enclosure than *ODH* does. This geometric adjustment allows heat to penetrate more effectively into the central PCM region. Consequently, during 7200 s and 10,800 s, the melted zones along the side walls grow while additional melting develops near the central region. The combined effects of heat conduction near the channel surfaces and natural convection in the melted PCM accelerate the melting process. By 14,400 s, only a small unmolten PCM region remains near the lower central section. At 18,000 s, the PCM in the *ODB* configuration is almost completely melted, showing a melting behavior that balances the rapid early melting of *ODH* with the more uniform late-stage melting of *ODF*.

In contrast, the core design exhibits significantly slower melting throughout the process because it lacks an inner HTF channel. Heat transfer occurs only from the outer HTF channel surrounding the enclosure. At 3600 s, melting is limited to a thin layer near the enclosure walls. Even at 7200 s and 10,800 s, the melted region remains mostly confined to the boundaries, while the majority of the PCM in the central region remains solid. The limited heat transfer area significantly restricts the development of natural convection, as only a small amount of PCM becomes liquid. As a result, the melting front progresses very slowly toward the interior. Even at 18,000 s, a significant part of the PCM stays in a solid state at the center, demonstrating the significant performance limitation of the reference configuration.

Fig. 11 presents the temperature distribution within the enclosure for the optimized and the core designs at different charging times. In all designs, the highest temperatures appear near the HTF channels. From these regions, heat propagates toward the colder PCM through a combination of thermal conduction in the solid phase and natural convection in the melted regions. In the *ODH* design, the temperature contours at 3600 s show that the PCM near both the outer and inner HTF channels is already significantly heated, while the central region remains relatively cold. Due to the larger inner channel height, heat is delivered more effectively to the upper regions of the enclosure, resulting in relatively high temperatures there. As the charging process progresses to 7200 s, the heated zones expand along the side walls and upper regions, while the central PCM region remains cooler due to its larger distance from the heat transfer surfaces. At 10,800 s and 14,400 s, the temperature gradients gradually diminish as the PCM melts and natural convection redistributes heat within the PCM. The warmer, lighter molten PCM rises under buoyancy forces, while relatively cooler PCM descends under

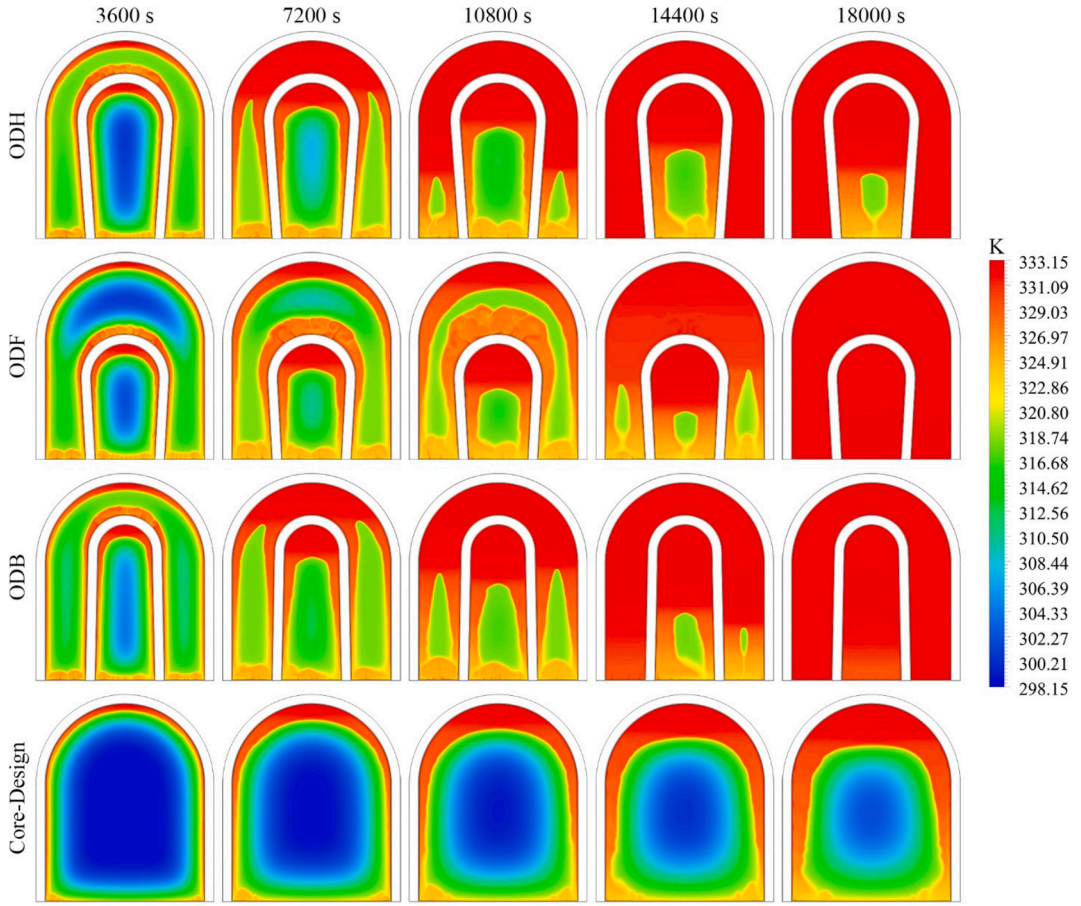

Fig. 11. Temperature contours for the optimized designs (ODH, ODF, and ODB) and the core design at different charging times.

gravity, generating a convective circulation that accelerates heat transport toward the interior. By 18,000 s, most of the PCM reaches temperatures close to the HTF temperature, although a small cooler region remains near the lower center.

The *ODF* configuration shows a slightly different thermal evolution due to its smaller inner HTF channel height, which positions the inner channel closer to the lower region of the enclosure. At 3600 s, high-temperature regions appear near the outer channel and the lower portions of the inner channel, while the upper PCM region is still comparatively cooler. As time progresses to 7200 s and 10,800 s, the heated regions extend upward along the outer walls, forming a large high-temperature zone near the top. The development of natural convection currents becomes more pronounced as larger liquid regions form, allowing heat to circulate more effectively throughout the enclosure. By 14,400 s, most of the PCM has reached temperatures near the melting point or above it, and by 18,000 s, the entire PCM domain becomes nearly uniform in temperature. The lower inner channel height in this configuration allows more PCM volume to occupy the enclosure, resulting in slightly slower initial heating but ultimately higher total stored energy.

The *ODB* configuration exhibits a temperature distribution that lies between those of *ODH* and *ODF*. At 3600 s, the temperature field shows significant heating near both HTF channels, similar to *ODH*, due to the relatively large channel height. However, the slightly smaller channel angle moves the inner HTF channel closer to the central region, thereby improving heat penetration into the PCM. At 7200 s and 10,800 s, the heated regions expand more uniformly across the enclosure compared with *ODH*, indicating improved heat distribution. As the molten PCM increases, buoyancy-driven convection strengthens, redistributing heat throughout the enclosure. By 14,400 s, only a small cooler region remains near the lower center, and at 18,000 s, the temperature becomes nearly uniform across the PCM domain, confirming the balanced thermal performance of the *ODB* design.

In contrast, the core design shows a much slower temperature evolution. Since this configuration lacks an inner HTF channel, heat is transferred only from the outer boundary of the enclosure. At 3600 s, the PCM near the walls begins to heat up while the central region remains almost entirely cold. Even at 7200 s and 10,800 s, the temperature increase is largely confined to a thin layer near the enclosure walls. The absence of internal heating surfaces significantly limits the development of natural convection, as the melted PCM region remains small for a long time. Consequently, heat penetration toward the center is very slow, and even at 18,000 s, a major fraction of the material remains at relatively low temperatures. This behavior clearly highlights the importance of the

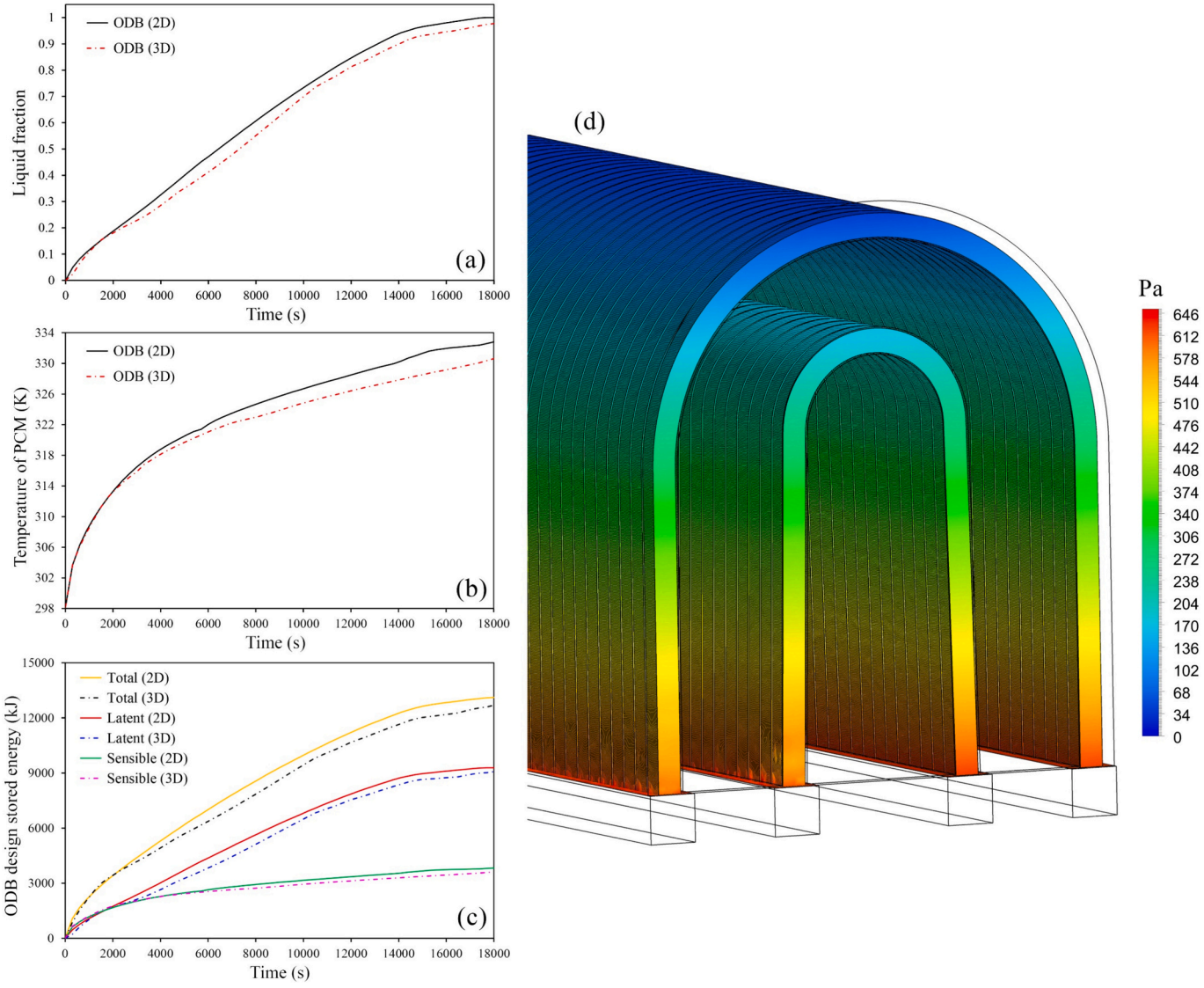

Fig. 12. Comparison between the 2D and 3D simulations for the optimal design (ODB). (a) Evolution of liquid fraction, (b) average PCM temperature, and (c) stored energy (total, latent, and sensible) during the charging process. (d) Pressure contour within the inner and outer HTF channels of the 3D model.

inner HTF channel in promoting heat transfer, accelerating PCM melting, and improving temperature uniformity within the enclosure.

10.4. 3D verification of the optimal design

A complete 3D transient simulation was performed for the optimal design (*ODB*) to evaluate the accuracy of the 2D modeling assumption adopted throughout this study. Owing to the complexity of the coupled fluid flow, heat transfer, and phase change, each 3D simulation required approximately five days of computational time. Therefore, conducting 3D simulations for all investigated configurations was computationally impractical. Instead, the optimal design was selected as a representative case for comparison. Figs. 12a-c compare the predictions of the 2D and 3D models in terms of liquid fraction, average PCM temperature, and stored energy. Excellent agreement is observed throughout the charging process. Both models predict nearly identical thermal responses, demonstrating that the 2D model accurately captures the dominant heat transfer and melting mechanisms governing the proposed storage system. Only slight deviations are observed, with the 3D model predicting marginally lower liquid fractions and stored energy during the charging process. This behavior is physically expected because the 3D model accounts for additional hydraulic effects and geometric complexities that are inherently neglected in the 2D approximation. Fig. 12d presents the pressure distribution within both the inner and outer HTF channels obtained from the 3D simulation. The total pressure drop between the inlet and outlet of the complete storage module is approximately 652 Pa. However, the pressure drop along an individual PCM unit is only about 2 Pa, indicating that frictional pressure losses along the longitudinal direction of each channel are very small. The majority of the overall pressure drop originates from repeated local pressure losses generated at the inlet of each parallel channel. As the HTF flows through the distribution manifold, it repeatedly divides into the smaller channels associated with each PCM unit. Each flow division introduces a local pressure loss, and the accumulation of these losses across all parallel units becomes the dominant contributor to the total pressure drop of the module. Consequently, although the complete 3D system exhibits a noticeable overall pressure drop, the longitudinal pressure loss within each individual unit remains negligible. This observation further supports the validity of the 2D assumption for investigating the thermal characteristics of the proposed device while significantly reducing the computational cost.

11. Conclusions

This work introduced a novel modular energy storage system inspired by plate heat exchanger architecture. In the proposed design, an additional HTF channel was embedded within the PCM enclosure to create two parallel heat transfer paths, thereby increasing the effective heat transfer area and improving thermal utilization of the PCM domain. To efficiently explore the design space, an MLP surrogate model was developed to predict the thermal energy stored during charging. The full factorial approach was implemented considering three independent design variables, namely the inner HTF channel height (*CH*), the spacing between the inlet and outlet of the inner HTF channel (*CS*), and the channel inclination angle (θ). The predictive model was then integrated with a two-stage optimization framework using a genetic algorithm and the TOPSIS decision-making method to identify optimal configurations that enhanced the system's charging performance. The key outcomes of this study are presented as follows:

- The results revealed substantial variation among the 27 modified designs, confirming that *CH*, *CS*, and θ were the key parameters and were properly selected to influence the heat absorption and melting process.
- The combination of a very high R^2 and a low RMSE demonstrated that the selected 3–7–2 MLP structure provided excellent predictive capability and served as a surrogate model for subsequent single- and multi-objective optimization procedures.
- *CH* was identified as the most influential parameter affecting the stored energy at 9000 s. Although *CS* and θ affected the melting behavior, their impact was secondary to that of the channel height during the intermediate charging stage.
- To maximize the stored energy at 9000 s, the GA identified an optimal configuration referred to as the Optimal Design for Half-time (*ODH*) with $CH = 280$ mm, $CS = 100$ mm, and $\theta = 94.08^{\circ}$.
- When the optimization objective was changed to maximizing the total stored energy at 18,000 s, the GA identified another optimal configuration, referred to as the Optimal Design for Full-time (*ODF*), with $CH = 205.705$ mm, $CS = 100$ mm, and $\theta = 93.18^{\circ}$.
- The TOPSIS method identified a balanced solution that simultaneously maintains high performance for both objectives. This configuration, referred to as the Optimal Design for the Balanced state (*ODB*), had geometric parameters of $CH = 280$ mm, $CS = 100$ mm, and $\theta = 88.8704^{\circ}$.
- At 9000 s, the liquid fractions were 0.6905, 0.5990, and 0.6721 for *ODH*, *ODF*, and *ODB*, respectively, whereas the core design reached only 0.1998. These values corresponded to improvements of approximately 245.6%, 199.8%, and 236.3%, respectively. At the same time, *ODH* stored the largest amount of energy (9402 kJ), followed by *ODB* (9287 kJ) and *ODF* (8654 kJ), whereas the core design stored only 3818 kJ. Accordingly, the stored energy increased by approximately 146%, 126.6%, and 143.2%, respectively.
- At 18,000 s, the liquid fractions reached 0.9649 for *ODH* and 1.0 for both *ODF* and *ODB*, while the core design reached only 0.3745. These values represented improvements of approximately 157.6%, 167.0%, and 167.0%, respectively. Moreover, *ODF* exhibited the highest stored energy (13,544 kJ), followed by *ODB* (13,113 kJ) and *ODH* (12,585 kJ). In contrast, the core design stored only 6457 kJ, corresponding to improvements of approximately 94.9%, 109.8%, and 103.1%, respectively.

CRediT authorship contribution statement

Yonghui Li: Investigation, Data curation. **Ali Basem:** Formal analysis, Data curation. **Mohammad Nadeem Khan:** Methodology, Conceptualization. **Teeba Ismail Kh:** Writing – original draft, Investigation. **Haibo Zhang:** Writing – review & editing, Supervision, Resources. **Norah Alsairy:** Validation, Formal analysis. **Ashrf Althbiti:** Validation, Data curation. **Zafar Rakhmanov:** Writing – review & editing, Writing – original draft. **Hind Albalawi:** Writing – review & editing, Supervision, Resources, Project administration. **Ibrahim Mahariq:** Supervision, Resources, Data curation.

Declaration of competing interest

The authors declare that they have no known competing financial interests or personal relationships that could have appeared to influence the work reported in this paper.

Acknowledgements

Princess Nourah bint Abdulrahman University Researchers Supporting Project number (PNURSP2026R29), Princess Nourah bint Abdulrahman University, Riyadh, Saudi Arabia. This work was financially supported by the Key Project of Philosophy and Social Sciences in Yunnan Province: "Research on Rule Coordination and Governance Innovation in China-Myanmar Cross-Border Data Flow (ZD202525)"; the National Social Science foundation project of China (23BJL088).

Data availability

The authors do not have permission to share data.

References

[1] A. Heras, J. Gupta, Fossil fuels, stranded assets, and the energy transition in the global south: a systematic literature review, WIREs Clim. Change 15 (2024), https://doi.org/10.1002/wcc.866.

[2] J. Wang, W. Azam, Natural resource scarcity, fossil fuel energy consumption, and total greenhouse gas emissions in top emitting countries, Geosci. Front. 15 (2024) 101757, https://doi.org/10.1016/j.gsf.2023.101757.

[3] G. Xia, X. He, Y. Jia, Y. Zhu, Z. Tian, Design of a cylindrical thermal rotary concentrator based on transformation thermodynamics, Materials (Basel) 18 (2025) 4440, https://doi.org/10.3390/ma18194440.

[4] H.M. Ali, T. Rehman, M. Arıcı, Z. Said, B. Duraković, H.I. Mohammed, et al., Advances in thermal energy storage: fundamentals and applications, Prog. Energy Combust. Sci. 100 (2024) 101109, https://doi.org/10.1016/j.pecs.2023.101109.

[5] H. Bahrami, M. Saberi, Thermal optimization of PCM-based heat sink using fins: a combination of CFD, genetic algorithms, and neural networks, J. Eng. Des. 2024 (2024), https://doi.org/10.1049/tje2.70015.

[6] J. Li, X. Chen, J. Shen, Y. Zhang, D. Liu, Optimal heat storage temperature and performance of ORC-based Carnot battery at various application scenarios, Energy Convers. Manag. 318 (2024) 118906, https://doi.org/10.1016/j.enconman.2024.118906.

[7] C.-H. Kim, M. Kim, Sholahudin, N. Giannetti, K. Saito, Systematic development of multilayer-perceptron-based void fraction model, Int. Commun. Heat Mass Transfer 162 (2025) 108563, https://doi.org/10.1016/j.icheatmasstransfer.2024.108563.

[8] Z.A.J. Ahmed, A.B.M. Ali, O. Al-Khatib, I. Mahariq, Numerical investigation of passive cooling enhancement using nano-encapsulated phase change materials in electronic thermal management systems, Therm. Sci. Eng. Prog. 65 (2025) 103965, https://doi.org/10.1016/j.tsep.2025.103965.

[9] S. Nekahi, F.S. Moghanlou, M. Vajdi, K. Vaferi, S. Nekahi, T. Gholizadeh, Development and performance evaluation of a honeycomb-structured shell-and-tube thermal storage system integrating a series of openings on the hexagonal cells for enhanced energy absorption/release, Int. Commun. Heat Mass Transfer 173 (2026) 110897, https://doi.org/10.1016/j.icheatmasstransfer.2026.110897.

[10] D. Kong, X. Tian, G. Li, C. Liu, X. Niu, S.A. Isaev, et al., Numerical study of particle deposition and heat transfer characteristics in an S-shaped miniature cooling channel of a gas turbine blade, Powder Technol. 468 (2026) 121612, https://doi.org/10.1016/j.powtec.2025.121612.

[11] L. Naik, V. Gumtapure, B.V. Rudra Murthy, Experimental investigation of melting and solidification characteristics in a vertical shell and tube latent heat thermal energy storage system with novel directional flow annular fins, J. Energy Storage 114 (2025) 115768, https://doi.org/10.1016/j.est.2025.115768.

[12] K. Narwal, R. Kempers, P.G. O'Brien, Enhanced energy storage density in thermal energy storage systems simultaneously heated with solar radiation and industrial waste heat, Results Eng. 25 (2025) 103792, https://doi.org/10.1016/j.rineng.2024.103792.

[13] J. Perumalsamy, S.B.M. Punniakodi, C. Selvam, R. Senthil, Enhancing phase change characteristics of hybrid nanocomposites for latent heat thermal energy storage, J. Compos. Sci. 9 (2025) 120, https://doi.org/10.3390/jcs9030120.

[14] S.A. Abdollahi, A. Basem, A. Alizadeh, D.J. Jasim, M. Ahmed, A.J. Sultan, et al., Combining artificial intelligence and computational fluid dynamics for optimal design of laterally perforated finned heat sinks, Results Eng. 21 (2024) 102002, https://doi.org/10.1016/j.rineng.2024.102002.

[15] Ye Lin, Guo Hao, Zhu Yinhai, Jiang Peixue, Large eddy simulation of film cooling flow from diffusion slot hole with crossflow coolant configuration, Phys. Fluids 35 (2023), https://doi.org/10.1063/5.0143002.

[16] H.E. Abdellatif, A. Belaadi, A. Arshad, M. Bourchak, Modeling and performance analysis of phase change materials in advanced thermal energy storage systems: a comprehensive review, J. Energy Storage 121 (2025) 116517, https://doi.org/10.1016/j.est.2025.116517.

[17] S. Liu, J. Han, Y. Shen, S.Y. Khan, W. Ji, H. Jin, et al., The contribution of artificial intelligence to phase change materials in thermal energy storage: from prediction to optimization, Renew. Energy 238 (2025) 121973, https://doi.org/10.1016/j.renene.2024.121973.

[18] P. B, A. T, P. Subramanian, N. Periyappan, A. Alarifi, M. Mariappan, Conch shell derived bio-carbon/Paraffin as novel composite phase change material with enhanced thermal energy storage properties for photovoltaic module cooling systems, Sol. Energy Mater. Sol. Cells 281 (2025) 113306, https://doi.org/10.1016/j.solmat.2024.113306.

[19] Q. Wang, D. Xiao, G. Tang, Z. Lu, X. Ge, C. Zou, et al., A latent-heat-coupled wellbore heat-transfer model with phase-change materials, Phys. Fluids 38 (2026), https://doi.org/10.1063/5.0324428.

[20] M. Sheng, H. Rong, C. Zhou, X. Sheng, X. Hu, X. Tang, et al., Simultaneously achieving high energy density, mechanical robustness, and closed-loop recyclability in phase change materials for advanced thermal energy systems, Adv. Energy Mater. (2026), https://doi.org/10.1002/aenm.70874.

[21] K. Balasubramanian, A.K. Pandey, Y.A. Bhutto, A. Islam, T. Kareri, S. Rahman, et al., Evolving thermal energy storage using hybrid nanoparticle: an experimental investigation on salt hydrate phase change materials for greener future, Energy Technol. 13 (2025), https://doi.org/10.1002/ente.202400248.

[22] K.A. Hammoodi, H.A. Hasan, M.H. Abed, A. Basem, A.M. Al-Tajer, Control of heat transfer in circular channels using oblique triangular ribs, Results Eng. 15 (2022) 100471, https://doi.org/10.1016/j.rineng.2022.100471.

[23] Z. Chen, X. Li, L. Chen, N. Huang, L. Liu, P. Du, et al., Parametric study and thermal-dynamic analysis on angles of leading bifurcations in double-layer microchannel heat sinks with nested impacting jet structure, Int. Commun. Heat Mass Transfer 175 (2026) 110945, https://doi.org/10.1016/j.icheatmasstransfer.2026.110945.

[24] K. Vaferi, A. Farajollahi, T. Gholizadeh, M. Rostami, Enhancing charging and discharging performance in a novel latent heat storage via design optimization and artificial neural network modeling, J. Energy Storage 114 (2025) 115757, https://doi.org/10.1016/j.est.2025.115757.

[25] G. Yan, J. Li, R.N. Dara, M. Shaban, R. Ghandour, F.M. Alhomayani, et al., Solar-powered compact thermal energy storage system with rapid response time and rib-enhanced plate via techniques of CFD, ANN, and GA, J. Energy Storage 105 (2025) 114807, https://doi.org/10.1016/j.est.2024.114807.

[26] Z. Han, S. Ding, Y. Wei, S. Ren, Experimental and numerical investigation on composite fins with different volumetric ratios in a shell-and-tube solar latent heat thermal energy storage device, Energy 347 (2026) 140483, https://doi.org/10.1016/j.energy.2026.140483.

[27] S. Tang, P. Liu, Y. Song, H. Xi, X. Wu, X. Yang, et al., Solidification performance enhancement of a latent heat thermal energy storage system: a novel discontinuous fin configuration for vertical shell-and-tube design, Renew. Energy 261 (2026) 125275, https://doi.org/10.1016/j.renene.2026.125275.

[28] J.-B. Mao, A. Basem, H.H. Abed Balla, O.J. Alkhatib, Y. Elmasry, Y. Li, et al., Triangular-rib structural mastery for enhanced latent heat storage system: artificial neural network optimization of geometry, orientation, and cost-effectiveness, J. Energy Storage 152 (2026) 120463, https://doi.org/10.1016/j.est.2026.120463.

[29] Z. Song, S. Wang, J. Hu, Y. Wang, X. Zhao, X. Yu, et al., Analysis on the effect of heat transfer fluid tube shape on topology optimization fin configuration and heat transfer characteristics of latent heat thermal energy storage systems, Int. Commun. Heat Mass Transfer 172 (2026) 110408, https://doi.org/10.1016/j.icheatmasstransfer.2025.110408.

[30] C. Prieto, E. Borri, M.C. Pavon-Moreno, G. Zsembinszki, L.F. Cabeza, A technical and economic comparison between concrete and latent thermal energy storage for concentrated solar power applications, Appl. Therm. Eng. 275 (2025) 126823, https://doi.org/10.1016/j.applthermaleng.2025.126823.

[31] F. Ren, P.-Z. Zhuang, X. Chen, H.-S. Yu, H. Yang, Physics-informed extreme learning machine (PIELM) for Stefan problems, Comput. Methods Appl. Mech. Eng. 441 (2025) 118015, https://doi.org/10.1016/j.cma.2025.118015.

[32] F.K. Chowdhury, M.S. Sami, M.J. Alam, A. Sayem, M.M.A. Khan, Machine learning-assisted NSGA-II-TOPSIS optimization of weld strength and processing time in fused deposition modeling, Results Eng. 29 (2026) 109365, https://doi.org/10.1016/j.rineng.2026.109365.

[33] X. Qu, T. Zhao, J. Cao, Improved AHP and dual-hidden layer adaptive regularized neural network model for the quantitative risk assessment of oil and gas pipelines, Reliab. Eng. Syst. Saf. 268 (2026) 112028, https://doi.org/10.1016/j.ress.2025.112028.

[34] H.E. Abdellatif, S.A. Khan, A. Belaadi, D. Ghernaout, Enhancing thermal energy storage: the impact of inclined enclosure geometry and artificial neural network based modeling on phase change material melting performance, J. Energy Storage 114 (2025) 115750, https://doi.org/10.1016/j.est.2025.115750.

[35] K. Vaferi, S. Nekahi, S. Nekahi, H. Ghaebi, Charging/discharging performance examination in a finned-tube heat storage tank: based on artificial neural network, pareto optimization, and numerical simulation, Case Stud. Therm. Eng. (2025) 106388, https://doi.org/10.1016/j.csite.2025.106388.

[36] P. Duan, A.M. Abed, R. Chaturvedi, S.F. Ahmad, T. Absalamov, M. Dahari, et al., Heat absorption/release efficiency betterment of phase change material inside a shell-and-tube latent heat storage system under six different conditions of tube and fins, J. Energy Storage 90 (2024) 111880, https://doi.org/10.1016/j.est.2024.111880.

[37] S. Sharma, N. Sellami, A.A. Tahir, T.K. Mallick, R. Bhakar, Performance improvement of a CPV system: experimental investigation into passive cooling with phase change materials, Energies 14 (2021) 3550, https://doi.org/10.3390/en14123550.

[38] W. Wagner, A. Pruß, The IAPWS formulation 1995 for the thermodynamic properties of ordinary water substance for general and scientific use, J. Phys. Chem. Ref. Data Monogr. 31 (2002) 387–535, https://doi.org/10.1063/1.1461829.

[39] E. Paccha-Herrera, W.R. Calderón-Muñoz, M. Orchard, F. Jaramillo, K. Medjaher, Thermal modeling approaches for a LiCoO2 Lithium-ion battery—a comparative study with experimental validation, Batteries 6 (2020) 40, https://doi.org/10.3390/batteries6030040.

[40] A.W. Kandeal, M. Ismail, A. Basem, M.M. Elsayad, W.H. Alawee, H.S. Majdi, et al., An overview of the improvement of natural convection heat transfer via surface thermal radiation for different geometries, Results Eng. 23 (2024) 102514, https://doi.org/10.1016/j.rineng.2024.102514.

[41] S. Riahi, W.Y. Saman, F. Bruno, M. Belusko, N.H.S. Tay, Impact of periodic flow reversal of heat transfer fluid on the melting and solidification processes in a latent heat shell and tube storage system, Appl. Energy 191 (2017) 276–286, https://doi.org/10.1016/j.apenergy.2017.01.091.

[42] C. Ma, D. You, J. Liu, M. Li, J. He, G. Totis, Topology optimization of cooling elements for worm wheel gear grinding machine tool bed under non-uniform heat sources, Appl. Therm. Eng. 281 (2025) 128739, https://doi.org/10.1016/j.applthermaleng.2025.128739.

[43] Z. Dong, C. Hu, X. Zhang, Y. Shen, X. Shen, J.I. Leon, Optimal energy management of buildings using neural network-based thermal prediction and economic model predictive control, Adv. Eng. Inform. 71 (2026) 104278, https://doi.org/10.1016/j.aei.2025.104278.

[44] H. Li, M. Sun, C. Nie, S. Wang, Q. Duan, C. Hu, et al., Branch design of annular fins for heat storage enhancement of the shell-and-tube latent heat thermal energy

storage unit, J. Energy Storage 124 (2025) 116904, https://doi.org/10.1016/j.est.2025.116904.
[45] A. Rabiea, T. Halawa, Investigation of the effect of eccentricity and shell diameter on the charging performance of erythritol for thermal energy storage, Case Stud. Therm. Eng. 65 (2025) 105648, https://doi.org/10.1016/j.csite.2024.105648.
[46] L.L. Hu, T.X. Yu, Mechanical behavior of hexagonal honeycombs under low-velocity impact – theory and simulations, Int. J. Solids Struct. 50 (2013) 3152–3165, https://doi.org/10.1016/j.ijsolstr.2013.05.017.
[47] J. Vogel, M. Johnson, Natural convection during melting in vertical finned tube latent thermal energy storage systems, Appl. Energy 246 (2019) 38–52, https://doi.org/10.1016/j.apenergy.2019.04.011.
[48] S. Qiu, P. Guo, C. Xu, E. Xia, B. Liao, L. Li, Research on engine compartment thermal management based on field synergy for enhanced convective heat dissipation, Case Stud. Therm. Eng. 77 (2026) 107508, https://doi.org/10.1016/j.csite.2025.107508.
[49] B. Kiyak, H.F. Oztop, N. Biswas, F. Selimefendigil, Effects of geometrical configurations on melting and solidification processes in phase change materials, Appl. Therm. Eng. 258 (2025) 124726, https://doi.org/10.1016/j.applthermaleng.2024.124726.
[50] J. Cheng, S. Jin, Z. Zheng, K. Hu, L. Yin, Y. Wang, Energy consumption prediction for water-based thermal energy storage systems using an attention-based TCN-LSTM model, Sustain. Cities Soc. 126 (2025) 106383, https://doi.org/10.1016/j.scs.2025.106383.
[51] M. Vajdi, K. Vaferi, Thermal–hydraulic performance analysis and optimization of a recuperator via geometric modification using numerical simulation and artificial neural networks, Results Eng. 30 (2026) 111058, https://doi.org/10.1016/j.rineng.2026.111058.
[52] B. Kamkari, D. Groulx, Experimental investigation of melting behaviour of phase change material in finned rectangular enclosures under different inclination angles, Exp. Thermal Fluid Sci. 97 (2018) 94–108, https://doi.org/10.1016/j.expthermflusci.2018.04.007.
[53] N. Kousha, M. Rahimi, R. Pakrouh, R. Bahrampoury, Experimental investigation of phase change in a multitube heat exchanger, J. Energy Storage 23 (2019) 292–304, https://doi.org/10.1016/j.est.2019.03.024.
[54] J.-W. Luo, K. Yaji, L. Chen, W.-Q. Tao, Data-driven multi-fidelity topology design of fin structures for latent heat thermal energy storage, Appl. Energy 377 (2025) 124596, https://doi.org/10.1016/j.apenergy.2024.124596.
[55] K. Wang, T. Wang, X. Li, Topology optimization of cooling channels based on swarm intelligence, Struct. Multidiscip. Optim. 68 (2025) 140, https://doi.org/10.1007/s00158-025-04076-x.
[56] L. Jiang, C. Liang, Z. Cheng, X. Wang, Y. Hao, X. Wang, et al., Preparation of high thermal conductivity form-stable phase change materials using nanoparticles for cold energy storage, J. Energy Storage 113 (2025) 115633, https://doi.org/10.1016/j.est.2025.115633.
[57] Z. Zheng, G. Yan, A.M. Abed, M.A. Alghassab, B. Abdullaeva, F.M. Alhomayani, et al., Optimizing and investigating the charging time of phase change materials in a compact-latent heat storage using pareto front analysis, artificial neural networks, and numerical simulations, J. Energy Storage 102 (2024) 113966, https://doi.org/10.1016/j.est.2024.113966.
[58] W. Deng, J. Li, S. Samad, A.M. Abed, A. Almadhor, S. Alhumaid, et al., Optimization and prediction of heat absorption in a modular multi-section latent heat storage system with dome-shaped components using a multilayer perceptron model, TOPSIS analysis, and Pareto fronts, J. Energy Storage 131 (2025) 117542, https://doi.org/10.1016/j.est.2025.117542.
[59] A. Basem, H.K. Abdulaali, A. Alizadeh, P.K. Singh, K. Parashar, A.E. Anqi, et al., Integrating artificial intelligence-Based metaheuristic optimization with Machine learning to enhance Nanomaterial-Containing latent heat thermal energy storage systems, Energy Convers. Manage.: X 25 (2025) 100835, https://doi.org/10.1016/j.ecmx.2024.100835.
[60] J. Li, W. Wang, Y. Deng, L. Gao, J. Bai, L. Xu, et al., Thermal performance analysis of composite phase change material of myristic acid-expanded graphite in spherical thermal energy storage unit, Energies 16 (2023) 4527, https://doi.org/10.3390/en16114527.
[61] A. Arif, V.S.N. Reddy, K. Srividya, U.T. Mallampalli, Utilizing multilayer perceptron for machine learning diagnosis in phase change material-based thermal management systems, Heat Transf. 53 (2024) 4922–4947, https://doi.org/10.1002/htj.23163.
[62] Z. Zhou, Z. Zhang, J. Zuo, K. Huang, L. Zhang, Phase change materials for solar thermal energy storage in residential buildings in cold climate, Renew. Sust. Energ. Rev. 48 (2015) 692–703, https://doi.org/10.1016/j.rser.2015.04.048.